

AD \_\_\_\_\_

Award Number: **DAMD17-98-1-8147**

TITLE: **Breast Cancer Screening Using Photonic Technology**

PRINCIPAL INVESTIGATOR: **Robert R. Alfano, Ph.D**

CONTRACTING ORGANIZATION: **City University of New York  
New York, New York 10031**

REPORT DATE: **September 2000**

TYPE OF REPORT: **Annual**

PREPARED FOR: **U.S. Army Medical Research and Materiel Command  
Fort Detrick, Maryland 21702-5012**

DISTRIBUTION STATEMENT: **Approved for Public Release;  
Distribution Unlimited**

The views, opinions and/or findings contained in this report are those of the author(s) and should not be construed as an official Department of the Army position, policy or decision unless so designated by other documentation.

**20010521 092**

REPORT DOCUMENTATION PAGE			Form Approved OMB No. 074-0188	
Public reporting burden for this collection of information is estimated to average 1 hour per response, including the time for reviewing instructions, searching existing data sources, gathering and maintaining the data needed, and completing and reviewing this collection of information. Send comments regarding this burden estimate or any other aspect of this collection of information, including suggestions for reducing this burden to Washington Headquarters Services, Directorate for Information Operations and Reports, 1215 Jefferson Davis Highway, Suite 1204, Arlington, VA 22202-4302, and to the Office of Management and Budget, Paperwork Reduction Project (0704-0188), Washington, DC 20503				
1. AGENCY USE ONLY (Leave blank)	2. REPORT DATE September 2000	3. REPORT TYPE AND DATES COVERED Annual (15 August 1999 - 14 August 2000)		
4. TITLE AND SUBTITLE  Breast Cancer Screening Using Photonic Technology		5. FUNDING NUMBERS  DAMD17-98-1-8147		
6. AUTHOR(S)  Robert R. Alfano, Ph.D.				
7. PERFORMING ORGANIZATION NAME(S) AND ADDRESS(ES)  City University of New York New York, New York 10031  E-Mail: alfano@scisun.sci.ccny.cuny.edu		8. PERFORMING ORGANIZATION REPORT NUMBER		
9. SPONSORING / MONITORING AGENCY NAME(S) AND ADDRESS(ES)  U.S. Army Medical Research and Materiel Command Fort Detrick, Maryland 21702-5012		10. SPONSORING / MONITORING AGENCY REPORT NUMBER		
11. SUPPLEMENTARY NOTES				
12a. DISTRIBUTION / AVAILABILITY STATEMENT Approved for Public Release; Distribution Unlimited			12b. DISTRIBUTION CODE	
<b>13. ABSTRACT (Maximum 200 Words)</b> <p>The research performed during the current reporting period included: (a) time-sliced and spectroscopic two-dimensional (2-D) near-infrared transillumination imaging of normal and cancerous <i>in vitro</i> human breast tissue specimens; (b) derivation of analytical solutions of the Boltzmann radiative transport equation; and (c) development of theoretical formalism and computer algorithm for three-dimensional (3-D) inverse image reconstruction method using back-propagating light.</p> <p>Images recorded with earlier temporal slices of transmitted light were found to highlight cancerous tissues while those recorded with later slices accentuated normal fibrous tissues. Initial spectroscopic imaging experiments show that the ratio, <i>R</i> of light intensity transmitted through the cancerous tissue to that through the corresponding normal tissue show a wavelength dependent variation that has the potential to be used as a useful parameter for cancer identification. The analytical solutions of the Boltzmann transport equation enable a more accurate description of the ballistic and snake components of light emerging from a highly-scattering medium than that afforded by the diffusion approximation. Inverse image reconstruction scheme using simulated backscattered light provides fast, noise-resistant 3-D images of objects at various depths up to 2 cm in a tissue-like scattering medium.</p>				
14. SUBJECT TERMS Breast Cancer, optical mammography, time-resolved imaging, inverse image reconstruction, spectroscopic imaging, transillumination			15. NUMBER OF PAGES 44	
			16. PRICE CODE	
17. SECURITY CLASSIFICATION OF REPORT Unclassified	18. SECURITY CLASSIFICATION OF THIS PAGE Unclassified	19. SECURITY CLASSIFICATION OF ABSTRACT Unclassified	20. LIMITATION OF ABSTRACT Unlimited	

NSN 7540-01-280-5500

Standard Form 298 (Rev. 2-89)  
Prescribed by ANSI Std. Z39-18  
298-102

### **(3) TABLE OF CONTENTS**

	<b>Page</b>
<b>1. Front Cover</b>	<b>1</b>
<b>2. SF 298</b>	<b>2</b>
<b>3. Table of Contents</b>	<b>3</b>
<b>4. Introduction</b>	<b>4</b>
<b>5. Body</b>	<b>4</b>
<b>5.1 Enhancement of spectroscopic imaging arrangement</b>	<b>4</b>
<b>5.2 Time-sliced and Spectroscopic Shadowgram Imaging of         Excised Human Breast Tissues</b>	<b>4</b>
<b>5.3 Analytical solution of Boltzmann transport equation</b>	<b>5</b>
<b>5.4 Development Inverse Image Reconstruction Method         using Backscattered Light</b>	<b>5</b>
<b>6. Key Research Accomplishments</b>	<b>5</b>
<b>7. Reportable Outcomes</b>	<b>6</b>
<b>8. Conclusions</b>	<b>6</b>
<b>9. References</b>	<b>7</b>
<b>10. Appendices</b>	
Appendix 1	Preprint: "Temporally and spectrally resolved ..."
Appendix 2	Reprint: "Analytical solution of the elastic ..."
Appendix 3	Reprint: "Cumulant solution of the elastic ..."
Appendix 4	Reprint: "Time-resolved optical diffuse tomography"

#### (4) INTRODUCTION

The goal of the proposed, "**Breast Cancer Screening Using Photonic Technology**" research project is to develop optical imaging techniques that make use of noninvasive near-infrared (NIR) light for obtaining two-dimensional (2-D) transillumination, and three-dimensional (3-D) tomographic images of cancerous lesions of human breast. The imaging method involves illuminating the specimen with ultrashort NIR pulses of laser light and construction of images using two approaches. The first, known as the **shadowgram** method, utilizes the image bearing component of the forward-transmitted light to form direct shadow images. The second, referred to as the **three dimensional (3-D) inverse reconstruction method**, makes use of the measured transmitted, forward-scattered or backscattered light intensity profiles, known or estimated optical properties of the sample, a model for light propagation through turbid media and a sophisticated computer algorithm to construct images of the interior structure of the specimen.

We made significant advances in developing both of these approaches. What is even more important, our spectroscopic imaging experiments with normal and cancerous human breast tissues reveal useful differences in optical images and is indicative of the diagnostic ability of the **spectroscopic imaging** method.

#### (5) BODY

The tasks performed and the progress made during the current reporting period may be broadly grouped as follows:

- 5.1 Enhancement of the spectroscopic imaging arrangement,
- 5.2 Time-sliced and spectroscopic shadowgram imaging with excised human breast tissues
- 5.3 Analytic solution of Boltzmann Transport Equation, and
- 5.4 Development of the inverse image reconstruction method using backscattered light.

We will briefly outline our accomplishments in each of these areas, and refer to appended publications (Appendices 1-4) for detailed description where applicable.

##### **5.1 Enhancement of the Spectroscopic Imaging Arrangement**

We have improved on the spectroscopic imaging arrangement that we assembled and used during the first reporting period by replacing the old 128x128 pixels NIR area camera with a new area camera equipped with a 320x240 pixels sensing element (Sensors Unlimited SU-320). The new camera has improved the resolution of the images that we obtain significantly. This is an extension of the Technical Objectives 2 and 3 (**TO 2, 3**).

##### **5.2 Time-sliced and Spectroscopic Shadowgram Imaging of Excised Human Breast Tissues**

We have continued to pursue the time-sliced and spectroscopic shadowgram imaging of excised normal and cancerous human breast tissues using the experimental arrangements developed during the first reporting period (**TO 5-7, Tasks 12, 14**). The breast tissue specimens with infiltrating ductal carcinoma, and infiltrating lobular carcinoma from patients of different ages were obtained from our collaborators at the Memorial Sloan Kettering Cancer Center and National Disease Research Interchange under an IRB approval at the City College of New York.

A very promising and interesting result of 2-D spectroscopic imaging experiment is the wavelength-dependent difference in light transmission through the cancerous and normal tissues (**TO 5-7, Tasks 15**). As a measure of this difference we monitored the ratio,  $R$  of light intensity transmitted through the cancerous tissue to that through the corresponding normal tissue. We

found the value of  $R$  to be 1.5 for 1225 nm and 1.2 for 1300 nm, a significant difference, for a breast tissue sample with poorly differentiated carcinoma, grade III, with sarcomatoid features.<sup>1</sup> The results are detailed in *Appendix 1*. We observed similar wavelength-dependent variation in  $R$  for breast tissue samples with ductal carcinoma, as well. We will pursue measurements involving normal tissues and tissues with different types and stages of cancer to examine if  $R$  can be a parameter whose values would be indicative of cancer.

The results of time-sliced 2-D imaging experiments are consistent with our earlier results<sup>2</sup> that light transited through the cancerous tissues faster than through the normal tissue. Consequently, images obtained with light in the earlier time slices highlighted the cancerous tissues, while those obtained with light in the later time slices highlighted the normal tissues. Time-sliced imaging can thus separate out normal and cancerous tissues in excised specimens. Some of these results are also presented in *Appendix 1*.

### 5.3 Analytical Solution of Boltzmann Transport Equation

Our theoretical endeavor (TO 4, Task 10; TO 8, task 18). has resulted in the derivation of analytical solution of the elastic Boltzmann Transport Equation in an infinite uniform isotropic medium with an arbitrary phase function.<sup>3,4</sup> This new approach provides a more accurate and exact description of photon transport through highly scattering media than the commonly used diffusion approximation that fails to adequately account for ballistic and snake photons.<sup>5</sup> The approach enables calculation of (a) the exact distribution in angle, and (b) the spatial cumulants at any angle, exact up to an arbitrary high-order (*Appendix 2*).<sup>3</sup> Terminating the cumulant expansion at the second order, we have derived an analytical solution of the distribution function, and density distribution (*Appendix 3*).<sup>4</sup> These expressions show a clear picture of time evolution of particle migration from ballistic to snake-like, then to diffusive regime. Use of these analytic solutions will provide more sophisticated 3-D inverse image reconstruction schemes.

### 5.4 Development Inverse Image Reconstruction Method using Backscattered Light

We have made another major advance in developing a novel inverse image reconstruction (IIR) method during this reporting period (TO 4, Tasks 8, 9; TO 8, Task 18). This new approach<sup>6</sup> uses backscattered photons from the scattering medium containing absorbing inhomogeneities, and differs from our earlier method<sup>7</sup> that used transmitted and forward scattered photons. It introduces the concept of propagation of spatial Fourier component of the scattered wave field inside the scattering medium, and then develops a new optical diffuse imaging methodology based on that theory. The method is fast and capable of providing 3-D image information. A test run using simulated data was able to reconstruct images of four inhomogeneities located up to 2 cm below the surface of a human tissue-like semi-infinite scattering medium using backscattered photons. *The inverse reconstruction method using backscattered light is detailed in the preprint of a paper presented here as Appendix 4*. We will pursue testing of this method<sup>6</sup> for inverse reconstruction of objects using experimental data, and compare the results with that obtained using the reconstruction method that used transmitted light.<sup>7</sup>

## (6) KEY RESEARCH ACCOMPLISHMENTS

- Obtained time-sliced 2-D transillumination images normal and cancerous tissues wherein images recorded with earlier temporal slices of transmitted light highlighted

cancerous tissues while those recorded with later slices accentuated normal fibrous tissues.

- Carried out spectroscopic imaging experiments and identified a ratio,  $R$  of light intensity transmitted through the cancerous tissue to that through the corresponding normal tissue show a wavelength dependent variation that has the potential to be used as a useful parameter for cancer identification.
- Developed analytical solutions of the Boltzmann transport equation that enable a more accurate description of the ballistic and snake components of light emerging from a highly-scattering medium than that afforded by the diffusion approximation.
- Developed the theoretical framework and computer algorithm for inverse image reconstruction scheme that would use backscattered light to provides fast, noise-resistant 3-D images of objects at various depths inside a scattering medium.

## (7) REPORTABLE OUTCOMES

### Articles

1. S. K. Gayen, M. Alrubaiee, M. E. Zevallos and R. R. Alfano, "Temporally and spectrally resolved optical imaging of normal and cancerous human breast tissues," in the *Proceedings of the Inter-Institute Workshop on In Vivo Optical Imaging at the NIH*, Edited by A. Gandjbakhche, Optical Society of America (to be published), p. 142.
2. W. Cai, M. Lax, and R. R. Alfano, "Analytical solution of the elastic Boltzmann transport equation in an infinite uniform medium using cumulant expansion," *J. Phys. Chem. B* **104**, 3996 (2000).
3. W. Cai, M. Lax, and R. R. Alfano, "Cumulant solution of the elastic Boltzmann transport equation in an infinite uniform medium," *Phys. Rev. E* **61**, 3871 (2000).
4. M. Xu, M. Lax, and R. R. Alfano, "Time-resolved optical diffuse tomography," *J. Opt. Soc. Am. A* (accepted for publication).

### Abstracts and Presentations

1. S. K. Gayen, M. Alrubaiee, R. R. Alfano, J. Koutcher, and H. Savage, "Electronic time-gated and spectroscopic near-infrared imaging of lesions in human tissues," *Bull. Am. Phys. Soc.* **45**, 958 (2000). Paper Y13 10 presented at the March Meeting of the American Physical Society, 20-24 March 2000, Minneapolis, MN.
2. S. K. Gayen, M. Alrubaiee, and R. R. Alfano, "Time-sliced and spectroscopic two-dimensional imaging of normal and cancerous human breast tissues," The Department of Defense Breast Cancer Research Program Meeting *Era of Hope*, Proceeding Volume I, p.195. Presented at the Hilton Atlanta and Towers, Atlanta, GA, June 8-11, 2000.
3. M. Xu, M. Lax, and R. R. Alfano, "Time-resolved Fourier diffuse optical tomography," in the Technical Digest of Biomedical Topical Meetings, TOPS Volume 38, Optical Society of America (2000) pp. 345-347. Paper TuC4 presented at the Biomedical Topical Meetings, Miami Beach, Florida, April 2-5, 2000.
4. W. Cai, M. Lax, and R. R. Alfano, "Analytical solution of the polarized photon transport equation in an infinite uniform scattering medium," in the Technical Digest of Biomedical Topical Meetings, TOPS Volume 38, Optical Society of America (2000) pp. 62-64. Paper TuC4 presented at the Biomedical Topical Meetings, Miami Beach, Florida, April 2-5, 2000.

## (8) CONCLUSIONS

The work carried out during this reporting period affirms some of our earlier inferences and leads to some new conclusions. *First*, time-sliced 2-D transillumination images recorded with earlier temporal slices of transmitted light highlighted cancerous tissues while those recorded with later slices accentuated normal fibrous tissues. *Second*, results of spectroscopic imaging experiments lead to a ratio,  $R$  of light intensity transmitted through the cancerous tissue to that has the potential to be used as a useful parameter for cancer identification. *Third*, analytical solutions of the Boltzmann transport equation that we obtained enable a more accurate description of the ballistic and snake components of light emerging from a highly-scattering medium than that afforded by the diffusion approximation. *Fourth*, the theoretical formalism and computer algorithm for inverse image reconstruction scheme using backscattered light shows (with simulated data) the potential to provide fast 3-D images of objects at various depths inside a scattering medium.

### **"So What Section"**

The implication of the first conclusion is that time-sliced imaging offers the possibility of highlighting cancerous lesions in human breast. The second conclusion points to the diagnostic potential of optical imaging, that of being able to diagnose a tumor as it is being imaged. X-ray mammography, most often used method, cannot diagnose cancer. The third and fourth conclusions together present the possibility of developing robust 3-D inverse image reconstruction formalisms, that in addition to being applicable for optical mammography, will be useful for imaging objects inside scattering media, such as, cloud, fog, smoke, and murky water.

## (9) REFERENCES

1. S. K. Gayen, M. Alrubaiee, M. E. Zevallos and R. R. Alfano, "Temporally and spectrally resolved optical imaging of normal and cancerous human breast tissues," in the *Proceedings of the Inter-Institute Workshop on In Vivo Optical Imaging at the NIH*, Edited by A. Gandjbakhche, Optical Society of America (to be published), p. 142.
2. S. K. Gayen and R. R. Alfano, "Sensing lesions in tissues with light," *Opt. Express* **4**, 475 (1999).
3. W. Cai, M. Lax, and R. R. Alfano, "Analytical solution of the elastic Boltzmann transport equation in an infinite uniform medium using cumulant expansion," *J. Phys. Chem. B* **104**, 3996 (2000).
4. W. Cai, M. Lax, and R. R. Alfano, "Cumulant solution of the elastic Boltzmann transport equation in an infinite uniform medium," *Phys. Rev. E* **61**, 3871 (2000).
5. S. R. Arridge and J. C. Hebden, "Optical imaging in medicine: II. Modeling and reconstruction," *Phys. Med. Biol.* **42**, 841 (1997).
6. M. Xu, M. Lax, and R. R. Alfano, "Time-resolved optical diffuse tomography," *J. Opt. Soc. Am. A* (accepted for publication).
7. W. Cai, S. K. Gayen, M. Xu, M. Zevallos, M. Alrubaiee, M. Lax, and R. R. Alfano, "Optical tomographic image reconstruction from ultrafast time-sliced transmission measurements," *Appl. Opt.* **38**, 4237 (1999).

## Appendix 1

*Proceedings of the Inter-Institute Workshop on In Vivo Optical Imaging at the NIH,*  
Edited by A. Gandjebache, Optical Society of America (to be published), p.142

### Temporally and spectrally resolved optical imaging of normal and cancerous human breast tissues

S. K. Gayen, M. Alrubaiee, M. E. Zevallos and R. R. Alfano

*Institute for Ultrafast Spectroscopy and Lasers, New York State Center for Photonic Materials and Applications, Departments of Physics and Electrical Engineering, The City College of the City University of New York, 138th Street at Convent Avenue, New York, NY 10031*  
[gayen@scisun.sci.ccny.cuny.edu](mailto:gayen@scisun.sci.ccny.cuny.edu), [alfano@scisun.sci.ccny.cuny.edu](mailto:alfano@scisun.sci.ccny.cuny.edu)

**Abstract:** Time-sliced and spectroscopic imaging arrangements were used to obtain two-dimensional (2-D) transillumination images of a composite *in vitro* human breast tissue sample comprising cancerous and normal fibrous tissues, adipose tissues, and a lymph node. Time-sliced imaging approach used 800-nm, approximately 130-fs duration, 1 kHz repetition-rate pulses from a Ti:sapphire laser system to illuminate the sample, and a gated imaging system that provided a variable-position, ~80 ps-duration electronic gate to record time-sliced 2-D images. Images recorded with earlier temporal slices (approximately, first 100 ps) of the transmitted light highlighted the lymph node and cancerous tissues, while the later slices (later than 300 ps) accentuated the adipose and normal tissues. Spectroscopic imaging arrangement made use of 1225 - 1300 nm light from a chromium-doped forsterite laser for sample illumination, a Fourier space gate and a polarization gate to sort out a fraction of the image-bearing photons, and an InGaAs area camera for recording 2-D images. Marked enhancement of image contrast between the adipose tissue and other tissues in the specimen was observed when the wavelength of imaging light was near resonant with the 1203-nm optical absorption resonance of the adipose tissue. Wavelength-dependent differences in relative light transmission through the normal and cancerous tissues were observed.

**OCIS codes:** (170.3880) Medical and biological imaging; (170.6920) time-resolved imaging; (290.7050) scattering, turbid media; (170.6510) spectroscopy, tissue diagnostics; (170.3660) light propagation in tissues; (999.999) Optical mammography; (999.999) near-infrared absorption spectroscopy of tissues; (999.999) spectroscopic imaging; (999.999) time-sliced imaging.

#### Introduction

Optical mammography, imaging of the interior structure of human breast with light, is an active area of optical biomedical imaging research.[1-4] Development of optical breast imaging modalities is of interest for several reasons. Optical imaging methods are noninvasive as no ionizing radiation is involved. Use of different wavelengths of light has the potential to provide diagnostic information. In contrast with x-ray mammography, light-based methods are as apt to image dense breast of a younger patient as that of an older patient. What is even more important, inverse image reconstruction methods using time-resolved or frequency-domain optical measurements may provide three-dimensional (3-D) tomographic breast images.[5-7] The ability to generate ultrashort pulses and color are two major attributes of light that may be exploited to develop an imaging modality with diagnostic ability.

In this article, we present the results of time-sliced[7] and spectroscopic[8] 2-D transillumination imaging measurements on excised human female breast tissue specimens comprising normal and cancerous tissues. Time-sliced imaging makes use of different temporal slices of the transmitted light to form 2-D images following the illumination of the sample with ultrashort near-infrared (NIR) pulses of light. The thrust of the spectroscopic imaging experiment is to examine if a spectroscopic difference

may be used to enhance image contrast, distinguish between different types of tissues in a specimen, and obtain diagnostic information.

## Methods and Materials

The time-sliced imaging arrangement used 800-nm, approximately 130-fs duration, 1 kHz repetition-rate pulses from a Ti:sapphire laser and amplifier system[9] for sample illumination, and an ultrafast gated intensified camera system (UGICS) for recording two-dimensional images using picosecond-duration slices of light transmitted through the sample. The UGICS comprised a compact time-gated image intensifier unit fiber-optically coupled to a charge-coupled device (CCD) camera. It provided a minimum gate width of approximately 80 ps whose temporal position could be varied in 25-ps steps over a 20-ns range. The average beam power used in the experiment was approximately 200 mW. The beam was expanded by a beam expander, and a 3-cm diameter central part of it was selected out using an aperture to illuminate the sample. The time-sliced image was recorded by the CCD camera and displayed on a computer.

The experimental arrangement for near-infrared (NIR) spectroscopic imaging made use of 1210-1300 nm continuous-wave mode-locked output of a  $\text{Cr}^{4+}$ :forsterite laser to illuminate the sample. A Fourier space gate[10] in conjunction with a polarization gate[11] selected out a fraction of the less-scattered image-bearing photons from the strong background of the image-blurring diffuse photons. A 50 mm focal-length camera lens placed on the optical axis at a distance of 50 mm from the aperture in the Fourier gate collected and collimated the low-spatial-frequency light filtered by the aperture and directed it to the 128x128 pixels sensing element of an InGaAs NIR area camera. The average optical power of the incident beam was maintained at approximately 35 mW for all the wavelengths used in the imaging experiment using appropriate neutral density filters. The laser beam was linearly polarized along the horizontal direction.

The composite excised breast tissue sample used in the experiments reported in this article was assembled from tissues obtained following the modified radical mastectomy of a 30-year-old patient. It comprised a lymph node (LN) with surrounding tissues, a piece of adipose (A) tissue, and a piece with normal (N) and cancerous (C) fibrous tissue. Each of the pieces was approximately 5 mm thick, and was pressed into a 5-mm thick quartz cell to ensure uniform sample thickness and good optical contact between the adjacent pieces. According to an accompanying surgical pathology report, the cancer was a poorly differentiated carcinoma, grade III with sarcomatoid features. Figure 1(a) shows a photograph of the exit face (the side that faces the camera in the experimental arrangements mentioned above) of the sample wherein the locations of different types of tissues in the composite sample are tentatively labeled. The tissues were made available to us by National Disease Research Interchange under an IRB approval from the City College of New York.

## Results

### *Time-sliced Imaging*

Time-sliced transillumination images of the sample for gate positions of 100 ps and 350 ps are displayed in Figs. 1(b) and 1(c), respectively. The zero position was taken to be the time of arrival of the light pulse through a 5-mm thick quartz cell filled with water. The spatial intensity profiles of the images in

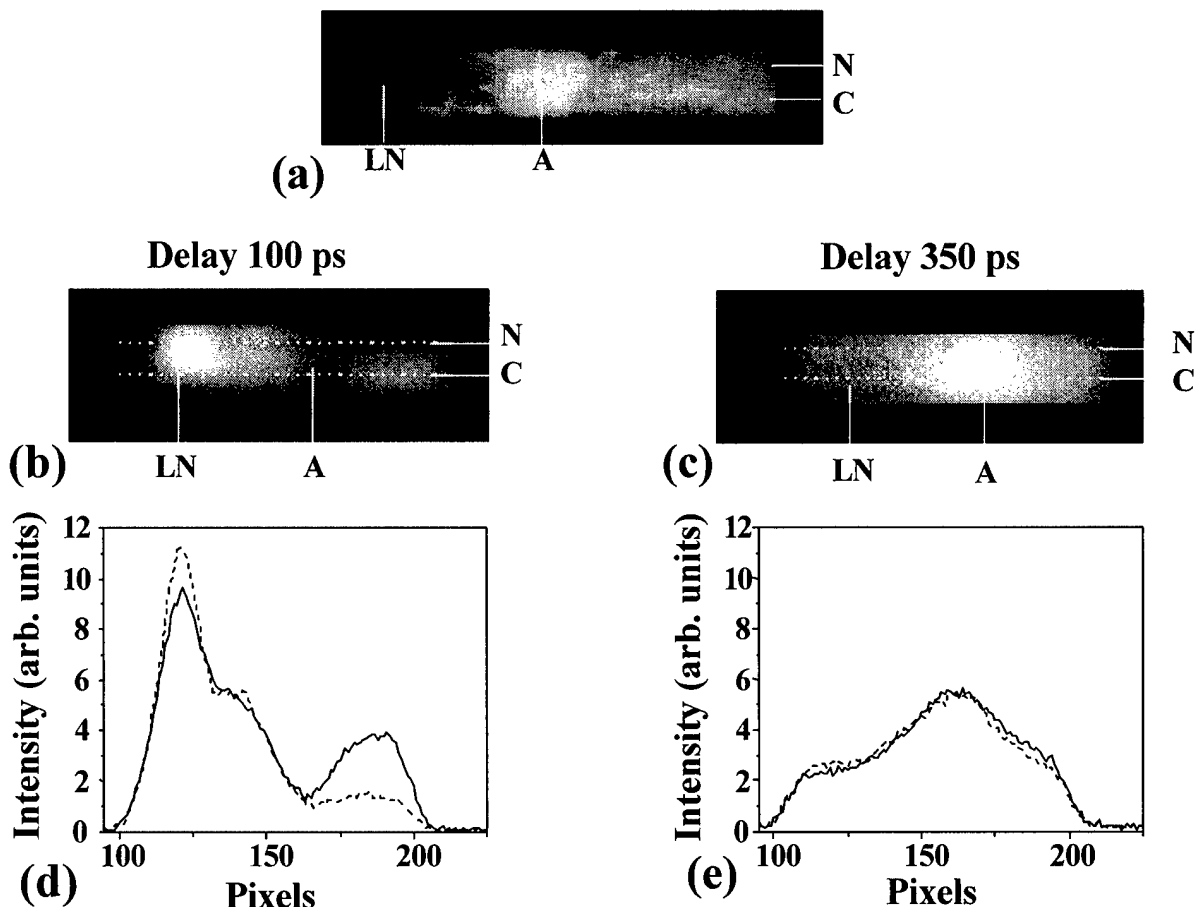


Figure 1.(a) A photograph of the exit face (the side that faces the camera in the experimental arrangements) of the composite breast tissue sample. LN, lymph node; A, adipose tissue; N, normal fibrous tissue; C, cancerous tissue. Time-sliced transillumination images of the sample for gate delays of (b) 100 ps, and (c) 350 ps. Spatial profile of the integrated intensity distribution along a horizontal area of 6 pixel vertical width around the dashed white line that passes through the normal fibrous tissue (dashed line), or the cancerous tissue (solid line) for a gate delay of (d) 100 ps, and (e) 350 ps.

Fig. 1(b) and Fig. 1(c) integrated over two 6-pixel wide horizontal areas around the white dashed lines are presented in Figs. 1(d) and 1(e), respectively. The two areas were chosen such that one included the normal fibrous tissue in the upper right part of the sample while the other included the cancerous tissue in the lower right part to enable close comparison. The time-sliced 100-ps image clearly highlights the lymph node, adipose, normal fibrous, and cancerous tissue regions. The contrast is the highest between the lymph node that appears the brightest and the adipose tissue that appears dark in the image. The spatial intensity distributions of the 100-ps image, displayed in Fig. 1(d), show the highest peak in intensity values in the lymph-node region and a marked trough in the adipose tissue region indicating much higher light transmission through the lymph node and much lower transmission through the adipose tissue region at early time. More interesting is the contrast between the cancerous and normal tissues in the 100-ps image. As seen in the right side of the image and the spatial intensity profiles of Fig. 1(d), light transmission through the cancerous tissue is significantly higher than that through the normal tissue.

A markedly different situation is observed in the 350-ps image of Fig. 1(c) and the corresponding spatial intensity profiles of Fig. 1(e). The adipose tissue region appears the brightest, and the spatial intensity profile peaks in the adipose tissue region indicating much higher light transmission through the

adipose tissue compared to transmission through other tissues in the sample at this later time. What is even more noteworthy, the difference in light transmission through the normal and cancerous regions that appeared so prominent in the profiles of Fig. 1(d) is not appreciable at this late time. It is reflected by the close overlapping of the two profiles in the regions of the normal and cancerous tissues in the profiles of Fig. 1(e). At intermediate times (not shown in figures) relative light transmission through the lymph node and cancerous tissues decreased while that through adipose and normal fibrous tissues increased with time. Summarizing the time-dependent transit of light, we find that the light transits fastest through the lymph node, followed by that through cancerous fibrous tissue, normal fibrous tissue, and the adipose tissue. Lower scattering or/and higher absorption of light by the lymph node and cancerous tissues may account for the observed temporal behavior. Since there is no known absorption of 800-nm light by breast tissues, we attribute these time-dependent differences in the relative light transmission through different types of human breast tissues to the differences in the light scattering characteristics of these tissues.

These results demonstrate that time-sliced imaging can highlight different types of tissues in a sample. What is even more important, it can highlight normal fibrous tissues from poorly differentiated carcinoma (grade III) with sarcomatoid features. It should be noted that more pronounced difference in light scattering characteristics between normal fibrous tissues and infiltrating ductal carcinoma was observed[12] than that observed in this study between normal fibrous tissues and poorly differentiated carcinoma (grade III) with sarcomatoid features. This in turn indicates that light transport characteristics will vary between tissues with different types of carcinoma, as well as between normal and cancerous tissues.

### *Spectroscopic Imaging*

A spectroscopic difference between different types of tissues in a specimen is expected to provide some distinguishable signature in a transillumination image. In order to test if this signature may be realized in practice, we obtained images of the sample with 1225-nm light that is near-resonant with the adipose tissue optical absorption resonance around 1203 nm,[13] as well as, with light of wavelengths away from the resonance. Figures 2(a) and 2(b) show a 'near-resonant image' recorded with 1225-nm light, and a typical 'nonresonant image' recorded with 1300-nm light, respectively. Figures 2(c) and 2(d) display the corresponding spatial intensity profiles. The solid line in each of these figures shows the profile integrated over a 6-pixel wide area around the long dashed line that runs the entire length of the corresponding image and includes the cancerous tissue region in the lower right part of the image. The dashed curve superimposed on the solid curve shows the profile integrated over a 6-pixel wide normal fibrous tissue area enclosed by the smaller box in the corresponding image. The solid and the dashed curves in the right side of the profiles thus enable comparison of light transport characteristics through normal and cancerous tissues in the specimen.

The salient features of the spectroscopic images and corresponding profiles are: (a) the adipose tissues appear much darker (less light transmission) than other tissues in the near-resonant 1225-nm image as compared to that in the off-resonance 1300-nm image; (b) cancerous tissues appear brighter (higher light transmission) than the normal tissues in both the images; (c) while the overall light transmission through the normal region remains approximately at the same level, that through the cancerous region is significantly higher at 1225 nm than at 1300 nm; (d) transmission through the lymph node exhibits a wavelength-dependent variation as well, being higher at 1225 nm than at 1300 nm. The change in image contrast was the maximum for the adipose tissue as the wavelength of imaging light was changed from 1225 to 1300 nm. Adipose tissue region appeared as a much deeper trough in the

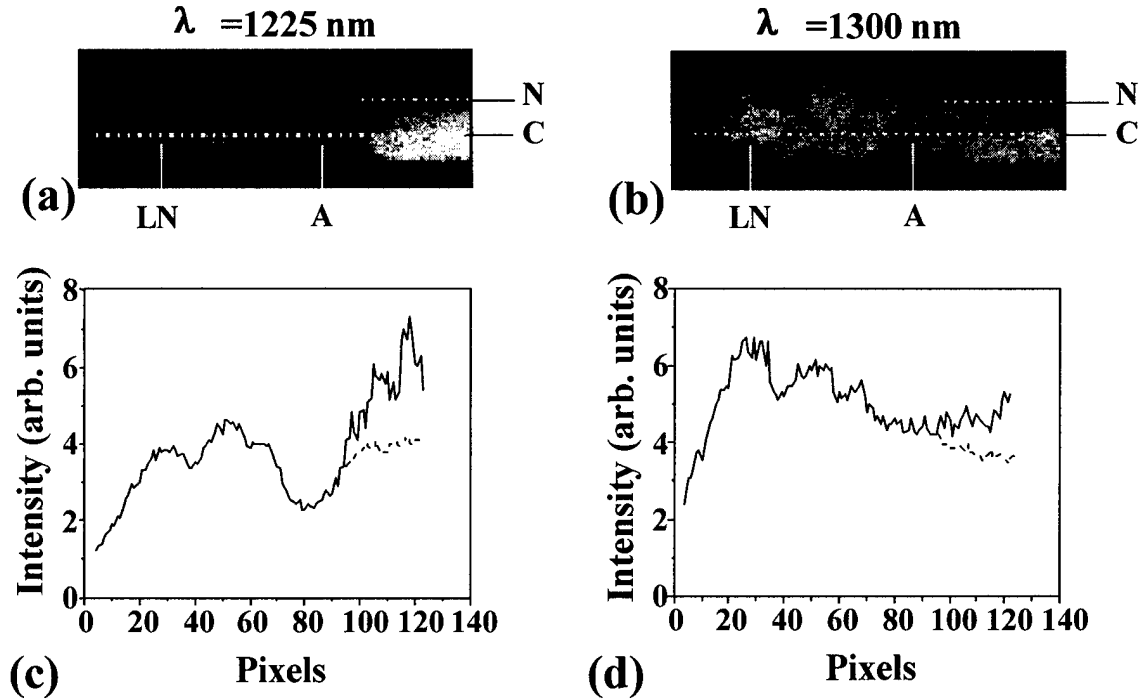


Figure 2. Spectroscopic 2-D transillumination image of the breast tissue sample described in the text for light of wavelength (a) 1225 nm, and (b) 1300 nm. Corresponding spatial profiles are shown in (c) and (d), respectively. Spatial profiles are the integrated intensity distribution along a 6-pixel wide horizontal area around the white dashed line covering the entire length of the sample including the cancerous tissue region (solid line in the profiles) and that around the small dashed line denoting the normal tissue region (broken line in the profiles).

spatial intensity profile of the 1225-nm image compared to that for the 1300-nm image. For a more quantitative description of the observed behavior, we monitored the image contrast,  $C(\lambda) = (I_F - I_A)/(I_F + I_A)$ , where  $I_A(\lambda)$  is the optimal intensity value at wavelength  $\lambda$  on the spatial profile of the image at the adipose tissue location, and  $I_F(\lambda)$  is the corresponding intensity in the immediate fibrous tissue region. Value of contrast at 1225 nm is 0.27 and 0.10 at 1300 nm. As the laser output was tuned away from 1225 nm to off-resonance wavelengths, the contrast between the adipose and fibrous regions in the images decreased from that maximum value of 0.27 towards 0.10. These results clearly demonstrate that an appreciable spectroscopic difference may significantly enhance the contrast between different types of breast tissues in a transillumination image, and is consistent with our previous results with adipose and fibrous human breast tissues.[8]

Even more promising and interesting is the wavelength-dependent difference in light transmission through the cancerous and normal tissues. As a measure of this difference we may monitor the ratio,  $R$  of light intensity transmitted through the cancerous tissue to that through the corresponding normal tissue. Taking the averaged intensity values[14] around the middle of the normal and cancerous tissues (Pixel # 110 in figures 2(c) and 2(d)), we obtain the value of  $R$  to be 1.5 for 1225 nm and 1.2 for 1300 nm, a significant difference. We observed similar wavelength-dependent variation in  $R$  for ductal carcinoma and normal breast tissue samples as well. More measurements involving normal tissues and tissues with different types and stages of cancer are needed to examine if  $R$  can be a parameter whose values would be indicative of cancer.

In summary, the spectroscopic and time-sliced imaging methods show tissue selectivity. A combined spectroscopic and time-sliced imaging approach has the potential to provide more information even than the x-ray techniques.

## Acknowledgements

We acknowledge J. Evans for technical help. The work is supported in part by the New York State Science and Technology Foundation, NASA IRA Program, USAMMRC, and DOE.

## References and Notes

1. M. Cutler, "Transillumination as an aid in the diagnosis of breast lesion," *Surg. Gynecol. Obstet.* **48**, 721-730 (1929).
2. E. Gratton, W. W. Mantulin, M. J. vande Ven, J. B. Fishkin, M. B. Maris, and B. Chance, "A novel approach to laser tomography," *Bioimaging*, **1**, pp. 40-46, 1993.
3. G. J. Muller, R. R. Alfano, S. R. Arridge, J. Beuthan, E. Gratton, M. Kaschke, B. R. Masters, S. Svanberg and P. van der Zee (editors), *Medical Optical Tomography: Functional Imaging and Monitoring*, Vol. IS 11, SPIE Institute Series, (SPIE, Bellingham, Washington, 1993).
4. L. Wang, P.P. Ho, G. Liu, G. Zhang, and R.R. Alfano, "Ballistic 2-D imaging through scattering walls using an ultrafast optical Kerr Gate", *Science* **253**, pp. 769-771, 1991.
5. For a recent review of the inverse reconstruction methods, see S. R. Arridge and J. C. Hebden, "Optical imaging in medicine: II. modeling and reconstruction," *Phys. Med. Biol.* **42**, 841-853 (1997).
6. M. A. O'Leary, D. A. Boas, B. Chance and A. G. Yodh, "Experimental images of heterogeneous turbid media by frequency-domain diffusing-photon tomography," *Opt. Lett.* **20**, 426-428 (1995).
7. W. Cai, S. K. Gayen, M. Xu, M. Zavallos, M. Alrubaiee, M. Lax and R. R. Alfano, "Optical tomographic image reconstruction from ultrafast time-sliced transmission measurements," *Appl. Opt.* **38**, 4237-4246 (1999).
8. S. K. Gayen, M. E. Zavallos, M. Alrubaiee, and R. R. Alfano, "Near-infrared laser spectroscopic imaging: a step towards diagnostic optical imaging of human tissues," *Laser Life Sci.* **8**, 187-198 (1999).
9. Q. Fu, F. Seier, S. K. Gayen and R. R. Alfano, "High-average-power kilohertz-repetition-rate sub-100-fs Ti:sapphire amplifier system," *Opt. Lett.* **22**, 712-714 (1997).
10. J. J. Dolne, K. M. Yoo, F. Liu and R. R. Alfano, "IR Fourier space gate and absorption imaging through random media," *Laser Life Sci.* **6**, 131-141 (1994).
11. S. G. Demos and R. R. Alfano, "Temporal gating in highly scattering media by the degree of optical polarization," *Opt. Lett.* **21**, 161-163 (1996).
12. S. K. Gayen and R. R. Alfano, "Sensing lesions in tissues with light," *Opt. Express* **4**, 475-480 (1999).
13. F. A. Marks, "Optical determination of the hemoglobin oxygenation state of breast biopsies and human breast cancer xenografts in nude mice," in *Proceedings of Physiological Monitoring and Early Detection Diagnostic Methods*, Thomas S. Mang and Abraham Katzir (eds.), SPIE **1641**, Bellingham, Washington, pp. 227-237, 1992.
14. A 5-point smoothed average of intensity values around Pixel #110 was used to reduce the effect of noise in determining the ratio.

## Analytical Solution of the Elastic Boltzmann Transport Equation in an Infinite Uniform Medium Using Cumulant Expansion<sup>†</sup>

W. Cai,\* M. Lax, and R. R. Alfano

*Institute for Ultrafast Spectroscopy and Lasers, New York State Center of Advanced Technology for Ultrafast Photonic Materials and Applications, Department of Physics, The City College and Graduate Center of City University of New York, New York, New York 10031*

*Received: December 20, 1999*

We study the analytical solution of the time-dependent elastic Boltzmann transport equation in an infinite uniform isotropic medium with an arbitrary phase function. We calculate (1) the exact distribution in angle, (2) the spatial cumulants at any angle, exact up to an arbitrary high order  $n$ . At the second order,  $n = 2$ , an analytical, hence extremely useful combined distribution in position and angle, is obtained as a function of time. This distribution is Gaussian in position, but not in angle. The average center and spread of the half-width are exact. By the central limit theorem the complete distribution approaches this Gaussian distribution as the number of collisions (or time) increases. The center of this distribution advances in time, and an ellipsoidal contour that grows and changes shape provides a clear picture of the time evolution of the particle migration from near ballistic, through snake-like, and into the final diffusive regime. This second-order cumulant approximation also provides the correct ballistic limit. Algebraic expressions for the  $n$ th order cumulants are provided. The number of terms grows rapidly with  $n$ , but our expressives are recursive and easily automated.

### I. Introduction

Search for an analytical solution of the time-dependent elastic Boltzmann transport equation has lasted for many years.<sup>1–3</sup> Besides being considered as a classical problem in fundamental research in statistical dynamics, a novel approach to an analytical solution of this equation may have applications in a broad variety of fields. To our knowledge, an exact solution, even in an infinite uniform medium, is available only for isotropic scattering case, given by E. H. Hauge,<sup>4</sup> in the form of a Fourier transform in space and Laplace transform in time. Based on the angular moment expansion with cut-off to certain order, the Boltzmann transport equation is transferred to a series of moment equations. In the lowest order, a diffusion equation is derived and its analytical solution in an infinite uniform medium is obtained for anisotropic scattering cases. This analytical solution has been broadly applied in many applications. For example, the solution of inverse problems in optical tomography, such as the location of a tumor in a woman's breast from the scattering of light pulses, requires the inversion of a weight matrix<sup>5</sup> obtained by convoluting two Green's functions of the forward scattering problem. The analytical solution of the diffusion equation has provided the needed Green's function. A similar procedure can be applied to other problems, such as using a laser to monitor cloud distributions, to detect objects inside a cloud, or the use of low-frequency sound to detect oil-bearing layers deep under water. The diffusion approximation fails at early times when the particle distribution is still highly anisotropic. The solutions of the diffusion equation or the telegrapher's equation do not produce the correct ballistic limit of particle propagation.<sup>6</sup> Numerical approaches, including the Monte Carlo method, are the main tools in solving the elastic Boltzmann equation; however, detailed solution of a five-dimensional Boltzmann

transport equation using a predominately numerical approach leads to prohibitive CPU times.

In this paper, we seek an analytical solution of the elastic Boltzmann transport equation in an infinite uniform medium. We assume that the phase function,  $P(\mathbf{s}, \mathbf{s}_0)$ , depends only on the scattering angle:  $P(\mathbf{s}, \mathbf{s}_0) = P(\mathbf{s} \cdot \mathbf{s}_0)$ , where the velocity  $\mathbf{v} = v\mathbf{s}$ ,  $\mathbf{s}$  is a unit vector of direction, and  $v$  is the (constant) speed in the medium. Under this assumption, we can handle an arbitrary phase function. We obtain the exact angular distribution as a function of time. Based on this solution, we use a cumulant expansion of the particle distribution,  $I(\mathbf{r}, \mathbf{s}, t)$ , and derive exact spatial cumulants up to an arbitrary high order at any angle and time. A cut-off at second order yields a simple analytical expressions for  $I(\mathbf{r}, \mathbf{s}, t)$ , as a function of position  $\mathbf{r}$ , angle  $\mathbf{s}$ , and time  $t$ , and the particle density distribution,  $N(\mathbf{r}, t)$ , as a function of position  $\mathbf{r}$  and time  $t$ . These spatial Gaussian distributions have the exact first cumulant (the position of center of the distribution) and the exact second cumulant (the half-width of spread of the distribution). After many scattering events have taken place, the law of large numbers (the central limit theorem) guarantees that the spatial Gaussian distribution that we calculate will become accurate in detail, since the higher cumulants become relatively small. At early times, the spread of the distribution is narrow, hence, the spatial distribution function can be claimed quantitatively accurate for many applications, in the sense that it has the correct mean position and the correct half-width of spread as a function of time. Measurement of the higher order cumulants could require measuring instruments of extreme resolution.

The remainder of this paper is organized as follows. Section II describes the derivation of formula: (1) obtaining an exact solution of the distribution in angle, (2) obtaining an exact formal solution in position and angle, (3) using the cumulant expansion to calculate the exact analytical expressions of cumulants up to an arbitrary high order, (4) describing the

<sup>†</sup> Part of the special issued "Harvey Scher Festschrift".

\* Corresponding author.

calculation of the particle distribution function using a spatial Fourier transform. Section III discusses using a cut-off at second order to produce explicit expressions of the distribution function and the density distribution. A brief discussion and summary then follows in Section IV. In the Appendix, we derive analytical formulas for evaluating integrals in eq 12.

## II. Derivation of Cumulants to an Arbitrary High Order

The elastic Boltzmann kinetic equation of particles, with magnitude of velocity  $v$ , for the distribution function  $I(\mathbf{r}, \mathbf{s}, t)$  as a function of time  $t$ , position  $\mathbf{r}$ , and direction  $\mathbf{s}$ , in an infinite uniform medium, from a point pulse light source,  $\delta(\mathbf{r} - \mathbf{r}_0) \delta(\mathbf{s} - \mathbf{s}_0) \delta(t - 0)$ , is given by<sup>3</sup>

$$\partial I(\mathbf{r}, \mathbf{s}, t) / \partial t + \mathbf{v} \cdot \nabla_{\mathbf{r}} I(\mathbf{r}, \mathbf{s}, t) + \mu_a I(\mathbf{r}, \mathbf{s}, t) = \mu_s \int P(\mathbf{s}, \mathbf{s}') [I(\mathbf{r}, \mathbf{s}', t) - I(\mathbf{r}, \mathbf{s}, t)] d\mathbf{s}' + \delta(\mathbf{r} - \mathbf{r}_0) \delta(\mathbf{s} - \mathbf{s}_0) \delta(t - 0) \quad (1)$$

where  $\mu_s$  is the scattering rate,  $\mu_a$  is the absorption rate, and  $P(\mathbf{s}', \mathbf{s})$  is the phase function, normalized to  $\int d\mathbf{s}' P(\mathbf{s}', \mathbf{s}) = 1$ . When the phase function depends only on the scattering angle in an isotropic medium, we can expand the phase function in Legendre polynomials with constant coefficients,

$$P(\mathbf{s}, \mathbf{s}') = \frac{1}{4\pi} \sum_l a_l P_l(\mathbf{s} \cdot \mathbf{s}') \quad (2)$$

We first study the dynamics of the distribution in direction space,  $F(\mathbf{s}, \mathbf{s}_0, t)$ , on a spherical surface of radius 1, which is equivalent to the velocity space in the elastic scattering case. The kinetic equation for  $F(\mathbf{s}, \mathbf{s}_0, t)$  can be obtained by integrating eq 1 over the whole spatial space,  $\mathbf{r}$ . The spatial independence of  $\mu_s$ ,  $\mu_a$ , and  $P(\mathbf{s}, \mathbf{s}')$  retains translation invariance. Thus the integral of eq 1 obeys

$$\partial F(\mathbf{s}, \mathbf{s}_0, t) / \partial t + \mu_a F(\mathbf{s}, \mathbf{s}_0, t) + \mu_s [F(\mathbf{s}, \mathbf{s}_0, t) - \int P(\mathbf{s}, \mathbf{s}') F(\mathbf{s}', \mathbf{s}_0, t) d\mathbf{s}'] = \delta(\mathbf{s} - \mathbf{s}_0) \delta(t - 0) \quad (3)$$

In contrast to eq 1, if we expand  $F(\mathbf{s}, \mathbf{s}_0, t)$  in spherical harmonics, its components do not couple with each other. Therefore, it is easy to obtain the exact solution of eq 3:<sup>7</sup>

$$F(\mathbf{s}, \mathbf{s}_0, t) = \exp(-\mu_a t) \sum_l \frac{2l+1}{4\pi} \exp(-g_l t) P_l(\mathbf{s} \cdot \mathbf{s}_0) = \exp(-\mu_a t) \sum_l \frac{2l+1}{4\pi} \exp(-g_l t) \sum_m Y_{lm}(\mathbf{s}) Y_{lm}^*(\mathbf{s}_0) \quad (4)$$

where  $g_l = \mu_s [1 - a_l / (2l+1)]$ . Two special values of  $g_l$  are  $g_0 = 0$ , which follows from the normalization of  $P(\mathbf{s}, \mathbf{s}')$  and  $g_1 = v/l_t$ , where  $l_t$  is the transport mean free path, defined by  $l_t = v / [\mu_s (1 - \overline{\cos \theta})]$ , where  $\overline{\cos \theta}$  is the average of  $\mathbf{s} \cdot \mathbf{s}'$  with  $P(\mathbf{s}, \mathbf{s}')$  as weight. In eq 4,  $Y_{lm}(\mathbf{s})$  are spherical harmonics. Equation 4 serves as the exact Green's function of particle propagation in velocity space. Since in an infinite uniform medium this function is independent of the source position,  $\mathbf{r}_0$ , requirements for a Green's function are satisfied, especially, a Chapman-Kolmogorov condition is obeyed:  $\int d\mathbf{s}' F(\mathbf{s}'', \mathbf{s}', t - t') F(\mathbf{s}', \mathbf{s}, t' - t_0) = F(\mathbf{s}'', \mathbf{s}, t - t_0)$ . In fact, in an infinite uniform medium, this propagator determines all particle migration behavior, including its spatial distribution, because displacement is an integration of velocity over time. The distribution function  $I(\mathbf{r},$

$\mathbf{s}, t)$  (the source is located at  $\mathbf{r}_0 = 0$ ) is given by

$$I(\mathbf{r}, \mathbf{s}, t) = \langle \delta(\mathbf{r} - \mathbf{v} \int_0^t \mathbf{s}(t') dt') \delta(\mathbf{s}(t) - \mathbf{s}) \rangle \quad (5)$$

where  $\langle \dots \rangle$  means the ensemble average in the velocity space. The first  $\delta$  function imposes that the displacement,  $\mathbf{r} - 0$ , is given by the path integral. The second  $\delta$  function assures the correct final value of direction. Equation 5 is an exact formal solution of eq 1, but can not be evaluated directly. We make a Fourier transform for the first  $\delta$ -function in eq 5, then make a cumulant expansion,<sup>8</sup> and obtain

$$I(\mathbf{r}, \mathbf{s}, t) = F(\mathbf{s}, \mathbf{s}_0, t) \frac{1}{(2\pi)^3} \int d\mathbf{k} \exp \left\{ i\mathbf{k} \cdot \mathbf{r} + \sum_{n=1}^{\infty} \frac{(-i\mathbf{v})^n}{n!} \sum_{j_n} \dots \sum_{j_1} k_{j_n} \dots k_{j_1} \langle \int_0^t dt_n \dots \int_0^{t_n} dt_1 T[s_{j_n}(t_n) \dots s_{j_1}(t_1)] \rangle_c \right\} \quad (6)$$

where  $T$  denotes time-ordered multiplication.<sup>9</sup> In eq 6, index  $c$  denotes cumulant, which is defined in many statistics textbooks,<sup>10</sup> as  $\langle A \rangle_c = \langle A \rangle$ ,  $\langle A^2 \rangle_c = \langle A^2 \rangle - \langle A \rangle \langle A \rangle$ , and a general expression relating  $\langle A^m \rangle$  and  $\langle A^m \rangle_c$ , which is given by:

$$\langle A^m \rangle = m! \sum_{m_1, m_2, \dots} \frac{1}{m_1!} \left( \frac{\langle A \rangle}{1!} \right)^{m_1} \frac{1}{m_2!} \left( \frac{\langle A^2 \rangle_c}{2!} \right)^{m_2} \dots \frac{1}{m_n!} \left( \frac{\langle A^n \rangle_c}{n!} \right)^{m_n} \times \delta(m - m_1 - 2m_2 - \dots - nm_n - \dots) \quad (7)$$

Hence, if  $\langle A^m \rangle$   $m = 1, 2, \dots, n$  have been calculated,  $\langle A^m \rangle_c$   $m = 1, 2, \dots, n$  can be recursively obtained and conversely.<sup>10</sup> In the following, we derive the analytical expression for the ensemble average  $\langle \int_0^t dt_n \dots \int_0^{t_n} dt_1 T[s_{j_n}(t_n) \dots s_{j_1}(t_1)] \rangle$ . Using a standard time-dependent Green's function approach, it is given by

$$\langle \int_0^t dt_n \dots \int_0^{t_n} dt_1 T[s_{j_n}(t_n) \dots s_{j_1}(t_1)] \rangle = \frac{1}{F(\mathbf{s}, \mathbf{s}_0, t)} \left\{ \int_0^t dt_n \int_0^{t_n} dt_{n-1} \dots \int_0^{t_2} dt_1 \int d\mathbf{s}^{(n)} \int d\mathbf{s}^{(n-1)} \dots \int d\mathbf{s}^{(1)} F(\mathbf{s}, \mathbf{s}^{(n)}, t - t_n) s_{j_n}^{(n)} F(\mathbf{s}^{(n)}, \mathbf{s}^{(n-1)}, t_n - t_{n-1}) s_{j_{n-1}}^{(n-1)} \dots F(\mathbf{s}^{(2)}, \mathbf{s}^{(1)}, t_2 - t_1) s_{j_1}^{(1)} F(\mathbf{s}^{(1)}, \mathbf{s}_0, t_1 - 0) + \text{perm} \right\} \quad (8)$$

where the word "perm" means all  $n! - 1$  terms obtained by permutation of  $\{j_i\}$ ,  $i = 1, \dots, n$ , from the first term. In eq 8,  $F(\mathbf{s}^{(i)}, \mathbf{s}^{(i-1)}, t_i - t_{i-1})$  is given by eq 4. Since eq 4 is exact, eq 8 provides the exact  $n$ th moments of the distribution. In Cartesian coordinates three components of  $\mathbf{s}$  are  $[s_x, s_y, s_z]$ . For convenience in calculation, however, we will use the components of  $\mathbf{s}$  on the basis of spherical harmonics:

$$\mathbf{s} = [s_1, s_0, s_{-1}] \equiv [Y_{11}(\mathbf{s}), Y_{10}(\mathbf{s}), Y_{1-1}(\mathbf{s})] = [-2^{-1/2} \sin \theta e^{+i\phi}, \cos \theta, +2^{-1/2} \sin \theta e^{-i\phi}]$$

The recurrence relation of the spherical harmonics is given by

$$Y_{lm}(\mathbf{s}) Y_{lj}(\mathbf{s}) = \sum_i Y_{l+i, m+j}(\mathbf{s}) \langle l, 1, m, j | l+i, m+j \rangle \times \langle l, 1, 0, 0 | l+i, 0 \rangle, i = \pm 1 \quad (9)$$

where  $\langle l_1, l_2, m_1, m_2 | l, m \rangle$  is the Clebsch-Gordan coefficients of angular momentum theory,<sup>11</sup> which are

$$\langle l-i, 1, m, j | l, m, j \rangle = \begin{bmatrix} \left[ \frac{(l-m)(l-m+1)}{(2l-1)2l} \right]^{1/2} & \left[ \frac{(l+m)(l-m+1)}{2l(l+1)} \right]^{1/2} & \left[ \frac{(l+m)(l+m+1)}{(2l+2)(2l+3)} \right]^{1/2} \\ \left[ \frac{(l-m)(l+m)}{(2l-1)l} \right]^{1/2} & \left[ \frac{m^2}{l(l+1)} \right]^{1/2} & -\left[ \frac{(l+m+1)(l-m+1)}{(l+1)(2l+3)} \right]^{1/2} \\ \left[ \frac{(l+m)(l+m+1)}{(2l-1)2l} \right]^{1/2} & -\left[ \frac{(l-m)(l+m+1)}{2l(l+1)} \right]^{1/2} & \left[ \frac{(l-m)(l-m+1)}{(2l+2)(2l+3)} \right]^{1/2} \end{bmatrix}$$

with the row index (from above)  $j = -1, 0, 1$  and the column index (from left)  $i = 1, 0, -1$ . The orthogonality relation of spherical harmonics is given by

$$\int ds Y_{lm}^*(s) Y_{lm}(s) = \frac{4\pi}{2l+1} \delta_{ll'} \delta_{mm'} \quad (10)$$

Using eqs 9 and 10, integrals over  $ds^{(n)} \dots ds^{(1)}$  in eq 8 can be analytically performed. We obtain, when  $s_0$  is set along  $z$ , that

$$\langle \int_0^t dt_n \dots \int_0^{t_n} dt_1 T[s_{j_n}(t_n) \dots s_{j_1}(t_1)] \rangle = \frac{1}{F(s, s_0, t)} \left\{ \sum_l Y_{[l \sum_{m=1}^n j_m]}(s) \sum_{i_n} \dots \sum_{i_1} \frac{2(l - \sum_{m=1}^n i_m) + 1}{4\pi} \times \right. \\ \left. D_{i_n \dots i_1}^l(t) \prod_{k=1}^n \langle l - \sum_{m=1}^{n-k+1} i_{n-m+1}, 1, \sum_{m=1}^{k-1} j_m, j_k | \right. \\ \left. l - \sum_{m=1}^{n-k} i_{n-m+1}, \sum_{m=1}^k j_m \rangle \langle l - \sum_{m=1}^{n-k+1} i_{n-m+1}, 1, 0, 0 | \right. \\ \left. l - \sum_{m=1}^{n-k} i_{n-m+1}, 0 \rangle \right\} + \text{perm} \quad (11)$$

where  $i_f = \pm 1, f = 1, 2, \dots, n$ , and

$$D_{i_n \dots i_1}^l(t) = \exp(-\mu_a t) \left\{ \int_0^t dt_n \int_0^{t_n} dt_{n-1} \dots \int_0^{t_2} dt_1 \exp[-g_l(t - t_n)] \right. \\ \left. \exp[-g_{l-i_n}(t_n - t_{n-1})] \dots \exp[-g_{l-\sum_{k=1}^n i_{n-k+1}}(t_1 - 0)] \right\} \quad (12)$$

Note that all ensemble averages have been performed. Equation 12 involves integrals of exponential functions, which can be analytically performed. An explicit expression for evaluating integrals in eq 12 is presented in the Appendix. Equation 12 includes all related scattering and absorption parameters,  $g_l, l = 0, 1, \dots$  and  $\mu_a$ , and determines the time evolution dynamics. The final particle direction,  $s$ , appears as argument of the spherical harmonics  $Y_{lm}(s)$  in eq 11. Substituting eq 12 into eq 11, and using a standard cumulant procedure, the cumulants as functions of angle  $s$  and time  $t$  up to an arbitrary  $n$ th order can be analytically calculated. The final position,  $r$ , appears in eq 6, and its component can be expressed as  $|r| Y_{lj}(\hat{r}), j = 1, 0, -1$ , with  $|r|$  and  $\hat{r}$  are, separately, magnitude and unit direction vector of  $r$ . Then, performing a numerical three-dimensional inverse Fourier transform over  $k$ , an approximate distribution function,  $I(r, s, t)$ , accurate up to  $n$ th cumulant, is obtained.

### III. Gaussian Approximation of the Distribution Function

By a cut-off at the second cumulant, the integral over  $k$  in eq 6 can be analytically performed, which directly leads to a Gaussian spatial distribution displayed in eq 13. The exact first cumulant provides the correct center position of the distribution.

The exact second cumulant provides the correct half-width of spread of the distribution. Moreover, the central limit theorem claims that as the number of collision events become large enough, the resulting Gaussian distribution approaches detailed accuracy beyond first two exact cumulants. At early time, spread of the spatial distribution is narrow, possibly narrower than the available detection instruments, hence, a spatial distribution with exact first and second cumulants may provide an accurate enough description of particle distribution for many applications.

For the reader's convenience, the expressions below are given in Cartesian coordinates with indices  $\alpha, \beta = [x, y, z]$ . These expression is obtained by use of an unitary transform  $s_\alpha = U_{\alpha j} s_j, j = 1, 0, -1$  from eq 11, (up to second order) which is based on  $s_j = Y_{lj}(s)$ , with

$$U = \begin{bmatrix} -2^{-1/2} & 0 & 2^{-1/2} \\ 2^{-1/2} i & 0 & 2^{-1/2} i \\ 0 & 1 & 0 \end{bmatrix}$$

We set  $s_0$  along the  $z$  direction and denote  $s$  as  $(\theta, \phi)$ . Our cumulant approximation to the particle distribution function is given by

$$I(r, s, t) = \frac{F(s, s_0, t)}{(4\pi)^{3/2}} \frac{1}{(\det B)^{1/2}} \exp \left[ -\frac{1}{4} (B^{-1})_{\alpha\beta} (r - r^c)_\alpha (r - r^c)_\beta \right] \quad (13)$$

with the center of the packet (the first cumulant), denoted by  $r^c$ , located at

$$r_z^c = G \sum_l A_l P_l(\cos \theta) [(l+1)f(g_l - g_{l+1}) + l f(g_l - g_{l-1})] \quad (14.1)$$

$$r_x^c = G \sum_l A_l P_l^{(1)}(\cos \theta) \cos \phi [f(g_l - g_{l-1}) - f(g_l - g_{l+1})] \quad (14.2)$$

where  $G = v \exp(-\mu_a t) F(s, s_0, t)$ ,  $A_l = (1/4\pi) \exp(-g_l t)$ ,  $g_l$  is defined after eq 4, and

$$f(g) = [\exp(g t) - 1]/g \quad (15)$$

$r_y^c$  is obtained by replacing  $\cos \phi$  in eq 14.2 by  $\sin \phi$ . In eq 14,  $P_l^{(m)}(\cos \theta)$  is the associated Legendre function.

The square of the average spread width (the second cumulant) is given by

$$B_{\alpha\beta} = v G \Delta_{\alpha\beta} - r_\alpha^c r_\beta^c / 2 \quad (16)$$

where all the coefficients are functions of angle and time:

$$\Delta_{zz} = \sum_l A_l P_l(\cos \theta) \left[ \frac{l(l-1)}{2l-1} E_l^{(1)} + \frac{(l+1)(l+2)}{2l+3} E_l^{(2)} + \frac{l^2}{2l-1} E_l^{(3)} + \frac{(l+1)^2}{2l+3} E_l^{(4)} \right] \quad (17.1)$$

$$\Delta_{xx,yy} = \sum_{l=2}^1 A_l P_l(\cos \theta) \left[ -\frac{l(l-1)}{2l-1} E_l^{(1)} - \frac{(l+1)(l+2)}{2l+3} E_l^{(2)} + \frac{l(l-1)}{2l-1} E_l^{(3)} + \frac{(l+1)(l+2)}{2l+3} E_l^{(4)} \right] \pm \sum_{l=2}^1 A_l P_l^{(2)}(\cos \theta) \cos(2\phi) \left[ \frac{1}{2l-1} E_l^{(1)} + \frac{1}{2l+3} E_l^{(2)} - \frac{1}{2l-1} E_l^{(3)} - \frac{1}{2l+3} E_l^{(4)} \right] \quad (17.2)$$

where (+) corresponds to  $\Delta_{xx}$  and (-) corresponds to  $\Delta_{yy}$

$$\Delta_{xy} = \Delta_{yx} = \sum_{l=2}^1 A_l P_l^{(2)}(\cos \theta) \sin(2\phi) \left[ \frac{1}{2l-1} E_l^{(1)} + \frac{1}{2l+3} E_l^{(2)} - \frac{1}{2l-1} E_l^{(3)} - \frac{1}{2l+3} E_l^{(4)} \right] \quad (17.3)$$

$$\Delta_{xz} = \Delta_{zx} = \sum_{l=2}^1 A_l P_l^{(1)}(\cos \theta) \cos \phi \left[ \frac{2(l-1)}{2l-1} E_l^{(1)} - \frac{2(l+2)}{2l+3} E_l^{(2)} + \frac{1}{2l-1} E_l^{(3)} + \frac{1}{2l+3} E_l^{(4)} \right] \quad (17.4)$$

$\Delta_{yz}$  is obtained by replacing  $\cos \phi$  in eq 17.4 by  $\sin \phi$ . In eq 17.1–17.4

$$E_l^{(1)} = [f(g_l - g_{l-2}) - f(g_l - g_{l-1})]/(g_{l-1} - g_{l-2}) \quad (18.1)$$

$$E_l^{(2)} = [f(g_l - g_{l+2}) - f(g_l - g_{l+1})]/(g_{l+1} - g_{l+2}) \quad (18.2)$$

$$E_l^{(3)} = [f(g_l - g_{l-1}) - t]/(g_l - g_{l-1}) \quad (18.3)$$

$$E_l^{(4)} = [f(g_l - g_{l+1}) - t]/(g_l - g_{l+1}) \quad (18.4)$$

A cumulant approximation for the particle density distribution is obtained from the exact expression  $N(\mathbf{r}, t) = \langle \delta(\mathbf{r} - \mathbf{v} \int_0^t \mathbf{s}(t') dt') \rangle$ . Using  $\int ds F(\mathbf{s}, \mathbf{s}', t) = \exp(-\mu_a t)$ , we have a Gaussian shape

$$N(\mathbf{r}, t) = \frac{1}{(4\pi D_{zz} vt)^{1/2}} \frac{1}{4\pi D_{xx} vt} \exp\left[-\frac{(z - R_z)^2}{4D_{zz} vt}\right] \times \exp\left[-\frac{(x^2 + y^2)}{4D_{xx} vt}\right] \exp(-\mu_a t) \quad (19)$$

with a moving center located at

$$R_z = v[1 - \exp(-g_1 t)]/g_1 \quad (20)$$

and the corresponding diffusion coefficients are given by

$$D_{zz} = \frac{v}{3t} \left\{ \frac{t}{g_1} - \frac{3g_1 - g_2}{g_1^2(g_1 - g_2)} [1 - \exp(-g_1 t)] + \frac{2}{g_2(g_1 - g_2)} [1 - \exp(-g_2 t)] - \frac{3}{2g_1^2} [1 - \exp(-g_1 t)]^2 \right\} \quad (21.1)$$

$$D_{xx} = D_{yy} = \frac{v}{3t} \left\{ \frac{t}{g_1} + \frac{g_2}{g_1^2(g_1 - g_2)} [1 - \exp(-g_1 t)] - \frac{1}{g_2(g_1 - g_2)} [1 - \exp(-g_2 t)] \right\} \quad (21.2)$$

In contrast to eqs 14 and 17, these results are independent of  $g_l$  for  $l > 2$ . Figure 1 shows the moving center of particles,  $R_z$  (eq 20), and the diffusion coefficients,  $D_{zz}$  and  $D_{xx}$  (eqs 21), as a function of time, where  $g_l$  is calculated by Mie theory of light scattering<sup>12</sup> assuming (for this figure) that the "uniform" scattering medium consists of water droplets with  $r/\lambda = 1$  are uniformly distributed in air, with  $r$  the radius of the droplet,  $\lambda$  the wavelength of light, and the index of refraction  $m = 1.33$ .

Each distribution in eqs 13 and 19 describes a particle "cloud" anisotropically spreading from a moving center, with time-dependent diffusion coefficients. At early time  $t \rightarrow 0$ ,  $f(g) \approx t + O(t^2)$  in eq 15, and  $E_l^{(j)} \approx t^2/2 + O(t^3)$  for  $j = 1, 2, 3, 4$  in eqs 18. From eqs 14, 17, and 20–21, we see that for the density distribution,  $N(\mathbf{r}, t)$ , and the dominant distribution function, that is  $I(\mathbf{r}, \mathbf{s}, t)$  along  $\mathbf{s} = \mathbf{s}_0$ , the center moves as  $vt \mathbf{s}_0$  and the  $B_{\alpha\beta}$  in eq 16 are proportional to  $t^3$  at  $t \rightarrow 0$ . A distribution function  $I(\mathbf{r}, \mathbf{s}, t)$  for  $\mathbf{s}$  not close to  $\mathbf{s}_0$  is small since  $F(\mathbf{s}, \mathbf{s}_0, t) \sim t$ , for small  $t$ . The center moves at a certain direction with displacement proportional to  $vt$ , and the  $B_{\alpha\beta}$  in eq 16 are proportional to  $t^2$  at  $t \rightarrow 0$ . These results present a clear picture of nearly ballistic motion at  $t \rightarrow 0$ . With increase of time, the motion of the center slows down, and the diffusion coefficients increase from zero. This stage of particle migration is often called a "snake-like mode".

With further increase in time, the  $l$ th Legendre component in eqs 4, 14, and 17, exponentially decays with a rate related to  $g_l$ . The detailed decay rate,  $g_l$ , is determined by the shape of the phase function. Generally speaking, the very high  $l$ th components decay in a rate of order of  $\mu_s$ , as long as its Legendre coefficient  $a_l$  distinctly smaller than  $2l + 1$ . Even in the case that the phase function has a very sharp forward peak, in which there are non-zero  $a_l$  for very high  $l$ th rank, the  $a_l$  are, usually, much smaller than  $2l + 1$ . Therefore, for the distribution function at time  $t$  after the ballistic stage is over, a truncation in summation of  $l$  is available.

At large times, the distribution function tends to become isotropic. From eqs 19–21, the particle density, at  $t \gg l/v$  and  $r \gg l$ , tends towards the conventional diffusion solution with the diffusive coefficient  $l/3$ . Therefore, our solution quantitatively describes how particles migrate from nearly ballistic motion to diffusive motion.

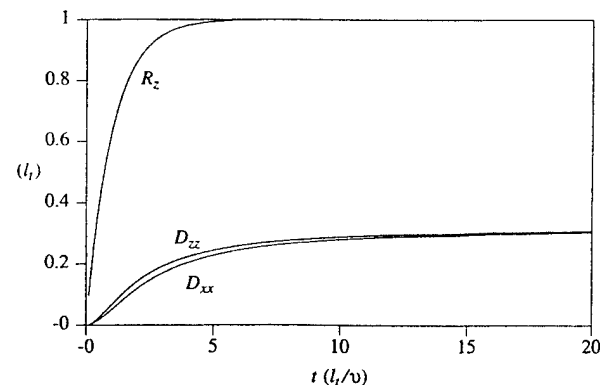


Figure 1. shows the moving center of a particle's density function,  $R_z$  (eq 20), and the diffusion coefficients,  $D_{zz}$  and  $D_{xx}$  (eqs 21), as functions of time,  $t$ .

#### IV. Discussion

The cumulant expansion terminating at the second order is a standard method in statistical mechanics,<sup>10</sup> which neglects cumulants higher than second order, and leads to a Gaussian distribution. If we examine the spatial displacement after each collision event as an independent random variable,  $\Delta \mathbf{r}_i$ , the total displacement is  $\sum \Delta \mathbf{r}_i$  ( $i = 1, \dots, N$ ), with  $N$  the number of collision events, which can be estimated by  $t/\mu_s$ . If we define  $\mathbf{Y} = (N)^{-1/2} \sum \Delta \mathbf{r}_i$ , the central limit theorem claims that if  $N$  is a large number, then  $\langle \mathbf{Y}^n \rangle_c / \langle \mathbf{Y}^2 \rangle_c \sim N^{1-n/2}$ ,  $n \geq 3$ . Therefore, the sum of  $N$  variables will have an essentially Gaussian distribution. Therefore, after enough collision events happened, the distributions we have calculated are accurate in detail, not just having the correct center and spread. At early time, the particle's spread is narrow, hence, in many applications the detailed shape is less important than the correct position and correct narrow width of the beam, because of the finite resolution of detection devices.

In case a more accurate distribution at early time is needed, by use of eqs 11 and 12 with its expression in Appendix, and a standard cumulant procedure, the exact higher (up to arbitrary  $n$ th) order cumulants can be analytically calculated. Then, performing a numerical three-dimensional Fourier transform, the particle distribution function accurate up to  $n$ th order cumulant approximation can be obtained.

In summary, we present an analytical solution of the elastic Boltzmann transport equation in an infinite uniform isotropic medium. Using a cumulant expansion we can analytically calculate cumulants up to an arbitrary high order. By terminating at the second order, we have derived an analytical solution of the distribution function, eq 13, and the density distribution, eq 19, with exact first cumulant (center of the distribution) and exact second cumulant (the half-width of spread of the distribution). These expressions show a clear picture of time evolution of particle migration from ballistic to snake-like, then to diffusion regime.

**Acknowledgment.** This work is supported in part by NASA, DOE, ARO, and New York State Science and Technology Foundation.

#### Appendix

In this Appendix, we derive an analytical expression of eq 12 to  $n$ th order. By defining

$$b_m = g_{[l - \sum_{k=1}^{n-m} i_{n-k+1}]} - g_{[l - \sum_{k=1}^{n-m+1} i_{n-k+1}]} \quad m = 1, \dots, n \quad (\text{A1})$$

eq 12 can be written as

$$D_{i_n \dots i_1}^l(t) = \exp(-\mu_a t) \exp(-g_l t) F^{(n)}(t) \quad (\text{A2})$$

with

$$F^{(n)}(t) = \int_0^t dt_n e^{b_n t_n} \int_0^{t_n} dt_{n-1} e^{b_{n-1} t_{n-1}} \dots \int_0^{t_2} dt_1 e^{b_1 t_1} \quad (\text{A3})$$

It is easy to directly calculate eq A3 for low  $n$  orders:

$$F^{(1)}(t) = \frac{e^{b_1 t}}{b_1} - \frac{1}{b_1} \quad (\text{A4.1})$$

$$F^{(2)}(t) = \frac{e^{(b_1+b_2)t}}{b_1(b_1+b_2)} - \frac{e^{b_2 t}}{b_1 b_2} + \frac{1}{(b_1+b_2)b_2} \quad (\text{A4.2})$$

$$F^{(3)}(t) = \frac{e^{(b_1+b_2+b_3)t}}{b_1(b_1+b_2)(b_1+b_2+b_3)} - \frac{e^{(b_2+b_3)t}}{b_1 b_2 (b_2+b_3)} + \frac{e^{b_3 t}}{(b_1+b_2)b_2 b_3} - \frac{1}{(b_1+b_2+b_3)(b_2+b_3)b_3} \quad (\text{A4.3})$$

In each step of integration, the difficulty is in determining the constant term. In the following we prove that this term is given by  $(-1)^n / [b_n(b_n+b_{n-1}) \dots (b_n+b_{n-1}+\dots+b_1)]$ . Equation A3 can be written as

$$F^{(n)}(t) = \int_0^t dt' e^{b_n t'} F^{(n-1)}(t') \quad (\text{A5})$$

Using integration by parts to eq A5, we obtain

$$F^{(n)}(t) = \frac{1}{b_n} [e^{b_n t} F^{(n-1)}(t) - \int_0^t dt' e^{(b_n+b_{n-1})t'} F^{(n-2)}(t')] \quad (\text{A6})$$

Recursively applying eq A6, we obtain

$$F^{(n)}(t) = \frac{e^{b_n t}}{b_n} F^{(n-1)}(t) - \frac{e^{(b_n+b_{n-1})t}}{b_n(b_n+b_{n-1})} F^{(n-2)}(t) + \dots + (-1)^k \frac{e^{(b_n+b_{n-1}+\dots+b_{n-k})t}}{b_n(b_n+b_{n-1}) \dots (b_n+b_{n-1}+\dots+b_{n-k})} F^{(n-k-1)}(t) + \dots + (-1)^{n-1} \frac{e^{(b_n+b_{n-1}+\dots+b_1)t} - 1}{b_n(b_n+b_{n-1}) \dots (b_n+b_{n-1}+\dots+b_1)} \quad (\text{A7})$$

Equation A7 provides formulas to recursively evaluate eq 12 up to  $n$ th order. Also, eq A7 produces the above mentioned constant term. An explicit expression of eq 12 can then be written as

$$D_{i_n \dots i_1}^l(t) = \exp(-\mu_a t) \exp(-g_l t) \sum_{m=0}^n \frac{(-1)^m \exp\left(\sum_{k=0}^{n-m} b_{n-k+1} t\right)}{\prod_{j=1}^n L_j^{(m)}} \quad (\text{A8})$$

with  $b_{n+1} \equiv 0$ , and

$$L_j^{(m)} = \sum_{k=j}^m b_k, j \leq m \text{ or } L_j^{(m)} = \sum_{k=m+1}^j b_k, j > m \quad (\text{A9})$$

#### References and Notes

- (1) Case, K. M.; Zweifel, P. F. *Linear Transport Theory*; Addison-Wesley: New York, 1967; and references contained.
- (2) Duderstadt, J. J.; Martin, W. R. *Transport Theory*; Wiley: New York, 1979; and references contained.
- (3) Chandrasekhar, S. *Radiative Transfer*; Oxford: New York, 1950; and references contained.
- (4) Hauge, E. H. In *Transport Phenomena*; Kirczenow, G., Marro, J., Eds.; Springer-Verlag: New York, 1974; pp 337–367.
- (5) Yodh, A. G.; Tromberg, B.; Seivick-Muraca, E.; Pine, D. J., Eds.; Diffusing photons in turbid media. Special issue of *J. Opt. Soc. Am. A* **1997**, *14*, 136–342; *Appl. Opt.* **1997**, *36*, 5–231.
- (6) Ishimaru, I. *Appl. Opt.* **1989**, *28*, 2210.
- (7) See, for example, Lax, M. *Rev. Mod. Phys.* **1960**, *32* (13), 25–64.
- (8) Wax, N. *Selected Papers on Noise and Stochastic Processes*; Dover: New York, 1954.
- (9) Feynman, R. P. *Phys. Rev.* **1951**, *84*, 108–128. Dyson, F. *Phys. Rev.* **1949**, *75*, 486–502.
- (10) Ma, S. H. *Statistical Mechanics*; World Scientific: Philadelphia, 1985.
- (11) Brink, D. M.; Satchler, G. R. *Angular momentum*; Clarendon Press: Oxford, 1962.
- (12) Bohren, C. F.; Huffman, D. R. *Absorption and Scattering of Light by Small Particles*; Wiley: New York, 1983.

## Cumulant solution of the elastic Boltzmann transport equation in an infinite uniform medium

W. Cai, M. Lax, and R. R. Alfano

*Institute for Ultrafast Spectroscopy and Lasers, New York State Center of Advanced Technology for Ultrafast Photonic Materials and Applications, Department of Physics, The City College and Graduate Center of City University of New York, New York, New York 10031*

(Received 16 October 1998; revised manuscript received 7 January 2000)

We consider an analytical solution of the time-dependent elastic Boltzmann transport equation in an infinite uniform isotropic medium with an arbitrary phase function. We obtain (1) the exact distribution in angle, (2) the exact first and second spatial cumulants at any angle, and (3) an approximate combined distribution in position and angle and a spatial distribution whose central position and half-width of spread are always exact. The resulting Gaussian distribution has a center that advances in time, and an ellipsoidal contour that grows and changes shape providing a clear picture of the time evolution of the particle migration from near ballistic, through snakelike and into the final diffusive regime.

PACS number(s): 42.25.Fx, 42.25.Dd, 78.90.+t, 0.5.20.-y

## I. INTRODUCTION

Scientists have tried for decades to develop exact or accurate analytical approximate solutions of the Boltzmann transport equation in various cases [1–3]. Any progress in this direction is a contribution to fundamental research in non-equilibrium statistical dynamics. An accurate analytical approximation may have applications in a broad range of fields, such as the atmosphere, medicine, and solid state physics. Photon migration in a highly scattering turbid medium is a good example. The solution of inverse problems in optical tomography, such as the location of a tumor in a woman's breast from the scattering of light pulses, requires the inversion of a weight matrix [4] obtained by convoluting two Green's functions of the forward scattering problem. The analytical solution of the photon diffusive equation in an infinite uniform medium has been broadly used as a background Green's function [4]. By introducing "image sources," the solution can be extended to semi-infinite, slabs, and boxes geometry. The diffusion approximation fails at early times when the photon distribution is highly anisotropic. Solutions of the diffusion equation or the telegrapher's equation do not produce the correct ballistic limit of light propagation [5]. The Monte Carlo method can be used to simulate photon migration at early times; however, detailed solution of a five-dimensional Boltzmann transport equation using a predominately numerical approach, with the resolution good enough to check the analytical solution, leads to prohibitive CPU times.

Recently, Polishchuk *et al.* [6] and Perelman *et al.* [7] suggested different models of photon migration. They used the path integral approach and the time-dependent Green's function method to treat the photon migration problem. They consider only multiple small-angle scattering, based on the fact that the phase function (angular distribution of the scattering cross section) in many media has a very sharp forward peak. A solution of the steady transport equation based on the small angle approximation was also presented by Ishimaru [8]. However, it can be shown that the transport mean free path obtained by an average of  $1 - \cos \theta$  over small angles could be several times larger than that obtained by an average over all angles. Thus, the small angle scattering ap-

proximation is not quantitatively correct. Therefore, a procedure permitting wide-angle scattering is essential.

In this paper, we present analytical expressions for the distribution function and the density distribution of the solution of the elastic Boltzmann transport equation in an infinite uniform medium. The phase function is assumed to depend only on the scattering angle  $P(s, s_0) = P(s \cdot s_0)$ . Under this assumption, the small angle approximation is avoided, and an arbitrary phase function can be handled. Our solution for the distribution in angle is exact, as are all first and second spatial cumulants at any angle as functions of time. After many scattering events have taken place, the central limit theorem guarantees that the spatial Gaussian distribution calculated will become accurate in detail, all cumulants higher than the second approach small values relative to the approximate power of the second cumulant. At early times, when the errors would be worst, the spatial distribution function at any angle is quantitatively accurate in the sense that it has the exact mean position (the first cumulant) and the exact and narrow half-width of spread (the second cumulant) as a function of time. Since the inverse scattering problem is done with instruments of finite resolution, in the presence of noise, finer detail is lost, and the first two cumulants may provide an adequate description of the scattered beam.

This paper is organized as follows. Section II describes the derivation of the formula, which includes (1) obtaining an exact solution of the distribution in angle, (2) obtaining an exact formal solution in position and angle, (3) using the cumulant approximation up to the second order that leads to a Gaussian spatial distribution, (4) obtaining exact first and second spatial cumulants based on the exact angular distribution. Section III provides the main results of the distribution function in position and angle, and the density distribution in position alone. Section IV makes a comparison of our result for the special case of isotropic scattering with that of the exact solution provided by Hauge [9]. A discussion of the effectiveness of the cumulant approximation is presented in Sec. V.

## II. DERIVATION

Without loss of generality, we discuss the photon scattering problem with a given light speed in the medium  $c$ . Ap-

plying our result to an another particle elastic scattering problem, with the constant particle speed in the medium  $v$  is straightforward. The photon distribution function  $I(\mathbf{r}, \mathbf{s}, t)$  as a function of time  $t$ , position  $\mathbf{r}$  and direction  $\mathbf{s}$ , in an infinite uniform medium, from a point pulse light source  $\delta(\mathbf{r} - \mathbf{r}_0)\delta(\mathbf{s} - \mathbf{s}_0)\delta(t - 0)$  obeys the Boltzmann equation [3]

$$\begin{aligned} \partial I(\mathbf{r}, \mathbf{s}, t) / \partial t + c \mathbf{s} \cdot \nabla_{\mathbf{r}} I(\mathbf{r}, \mathbf{s}, t) + \mu_a I(\mathbf{r}, \mathbf{s}, t) \\ = \mu_s \int P(\mathbf{s}, \mathbf{s}') [I(\mathbf{r}, \mathbf{s}', t) - I(\mathbf{r}, \mathbf{s}, t)] d\mathbf{s}' \\ + \delta(\mathbf{r} - \mathbf{r}_0) \delta(\mathbf{s} - \mathbf{s}_0) \delta(t - 0), \end{aligned} \quad (1)$$

where  $\mu_s$  is the scattering rate,  $\mu_a$  is the absorption rate, and  $P(\mathbf{s}', \mathbf{s})$  is the phase function, normalized to  $\int d\mathbf{s}' P(\mathbf{s}', \mathbf{s}) = 1$ . When the phase function depends only on the scattering angle in an isotropic medium, we can expand the latter in Legendre polynomials

$$P(\mathbf{s}, \mathbf{s}') = \frac{1}{4\pi} \sum_l a_l P_l(\mathbf{s} \cdot \mathbf{s}'), \quad (2)$$

and regard  $a_l$  as known, either from Mie theory [10], or a preliminary experiment.

We first study the dynamics of the photon distribution in the light direction space  $F(\mathbf{s}, \mathbf{s}_0, t)$ , on a spherical surface for  $\mathbf{s}$  of radius 1, which is equivalent to the velocity space in the elastic scattering case. The kinetic equation for  $F(\mathbf{s}, \mathbf{s}_0, t)$  can be obtained by integrating Eq. (1) over the whole space  $\mathbf{r}$ . The spatial independence of  $\mu_s$ ,  $\mu_a$ , and  $P(\mathbf{s}, \mathbf{s}')$  retains translation invariance. Thus the integral of Eq. (1) obeys

$$\begin{aligned} \partial F(\mathbf{s}, \mathbf{s}_0, t) / \partial t + \mu_a F(\mathbf{s}, \mathbf{s}_0, t) \\ + \mu_s \left[ F(\mathbf{s}, \mathbf{s}_0, t) - \int P(\mathbf{s}, \mathbf{s}') F(\mathbf{s}', \mathbf{s}_0, t) d\mathbf{s}' \right] \\ = \delta(\mathbf{s} - \mathbf{s}_0) \delta(t - 0). \end{aligned} \quad (3)$$

Since the integral of the gradient term over all-space vanishes, in contrast to Eq. (1), if we expand  $F(\mathbf{s}, \mathbf{s}_0, t)$  in spherical harmonics, its components do not couple with each other. Therefore, it is easy to obtain the exact solution of Eq. (3) [11]:

$$F(\mathbf{s}, \mathbf{s}_0, t) = \sum_l \frac{2l+1}{4\pi} \exp(-g_l t) P_l(\mathbf{s} \cdot \mathbf{s}_0) \exp(-\mu_a t), \quad (4)$$

where  $g_l = \mu_s [1 - a_l / (2l+1)]$ . Two special values of  $g_l$  are  $g_0 = 0$ , which follows from the normalization of  $P(\mathbf{s}, \mathbf{s}')$  and  $g_1 = c/l_t$ , where  $l_t$  is the transport mean free path, defined by  $l_t = c / [\mu_s (1 - \cos \theta)]$ , where  $\cos \theta$  is the average of  $\mathbf{s} \cdot \mathbf{s}'$  with  $P(\mathbf{s}, \mathbf{s}')$  as weight. Equation (4) serves as the exact Green's function of light propagation in the velocity (or angular) space. Since in an infinite uniform medium this function is independent of the source position  $\mathbf{r}_0$ , requirements for a Green's function are satisfied, especially, a Chapman-Kolmogorov condition is obeyed:  $\int d\mathbf{s}' F(\mathbf{s}'', \mathbf{s}', t - t') F(\mathbf{s}', \mathbf{s}, t' - t_0) = F(\mathbf{s}'', \mathbf{s}, t - t_0)$ . In fact, in an infinite uniform medium, this propagator determines all behavior of light migration, including its spatial distribution, because dis-

placement is an integration of velocity over time. The photon distribution function  $I(\mathbf{r}, \mathbf{s}, t)$ , for the initial source direction  $\mathbf{s}_0$  and the source position  $\mathbf{r}_0 = 0$ , is given by

$$I(\mathbf{r}, \mathbf{s}, t) = \left\langle \delta \left[ \mathbf{r} - c \int_0^t \mathbf{s}(t') dt' \right] \delta [\mathbf{s}(t) - \mathbf{s}] \right\rangle, \quad (5)$$

where the angle brackets denote the ensemble average in the velocity space. The first  $\delta$  function insures that the displacement,  $\mathbf{r} - 0$ , is given by the path integral. The second  $\delta$  function assures the correct final value of direction. Equation (5) is a formally exact solution, but can not be evaluated directly. We, hence, make a Fourier transform for the first  $\delta$  function in Eq. (5) and make a cumulant expansion to the second order [12]. For an arbitrary random variable,

$$\langle e^A \rangle \approx \exp(\langle A \rangle) \exp(\langle A^2 \rangle_c / 2), \quad (6)$$

where index  $c$  denotes cumulant:  $\langle A^2 \rangle_c = \langle A^2 \rangle - \langle A \rangle \langle A \rangle$ . An exact result is valid only if  $A$  is Gaussian. In the following  $\langle B \rangle_c$  is called the cumulant of  $B$ , while  $\langle B \rangle$  is called the moment of  $B$ . Substituting this approximation into the Fourier transform of Eq. (5), we have

$$\begin{aligned} I(\mathbf{r}, \mathbf{s}, t) = F(\mathbf{s}, \mathbf{s}_0, t) \frac{1}{(2\pi)^3} \int d\mathbf{k} \\ \times \exp \left( i k_\alpha \left( r_\alpha - c \left\langle \int_0^t dt' s_\alpha(t') \right\rangle \right) \right) \\ - \frac{1}{2} k_\alpha k_\beta c^2 \left\{ \left\langle \int_0^t dt' \int_0^t dt'' T[s_\alpha(t') s_\beta(t'')] \right\rangle \right. \\ \left. - \left\langle \int_0^t dt' s_\alpha(t') \right\rangle \left\langle \int_0^t dt' s_\beta(t') \right\rangle \right\}, \end{aligned} \quad (7)$$

where  $T$  denotes time-ordered multiplication [13]. Integration over  $\mathbf{k}$  in Eq. (7) directly leads to a Gaussian spatial distribution displayed in Eq. (10) below. Using a standard time-dependent Green's function approach, the ensemble average of the cumulants in Eq. (7) can be calculated. The components of the first cumulant, which is the average center position of the distribution, conditioned on  $\mathbf{s} = \mathbf{s}_0$  at  $t = 0$  are given by

$$\begin{aligned} \left\langle \int_0^t dt' s_\alpha(t') \right\rangle = \frac{1}{F(\mathbf{s}, \mathbf{s}_0, t)} \int_0^t dt' \int d\mathbf{s}' F(\mathbf{s}, \mathbf{s}', t - t') \\ \times s'_\alpha F(\mathbf{s}', \mathbf{s}_0, t'). \end{aligned} \quad (8)$$

The denominator appears because this is a conditional average. The components of the second moment, which is related to the second cumulant (average half-width of spread) of the distribution, conditioned on  $\mathbf{s} = \mathbf{s}_0$  at  $t = 0$  are given by

$$\begin{aligned}
& \left\langle \int_0^t dt' \int_0^t dt'' T[s_\alpha(t') s_\beta(t'')] \right\rangle \\
&= \frac{1}{F(s, s_0, t)} \left\{ \int_0^t dt' \int_0^t dt'' \int ds' \right. \\
&\quad \times \int ds'' F(s, s', t-t') s'_\alpha F(s', s'', t'-t'') \\
&\quad \times s''_\beta F(s'', s_0, t'') + (\text{t.c.}) \left. \right\}, \quad (9)
\end{aligned}$$

where (t.c.) means the second term is obtained by exchanging the index  $\alpha$  and  $\beta$  in the first term. Equation (7) is the only approximate formula used in our derivation. Formula for calculating the first two moments, Eqs. (8) and (9), are exact. In Eqs. (8) and (9),  $F(s_2, s_1, t)$  is given by Eq. (4). Since Eq. (4) is exact, Eqs. (8) and (9) provide the exact first and second moments. Integrations in Eqs. (8) and (9) are tedious, but straightforward.

### III. RESULTS

In the following, we set  $s_0$  along the  $z$  direction and denote  $s$  as  $(\theta, \phi)$ . Our cumulant approximation to the photon distribution function is given by

$$\begin{aligned}
I(\mathbf{r}, s, t) &= \frac{F(s, s_0, t)}{(4\pi)^{3/2}} \frac{1}{(\det B)^{1/2}} \exp \left[ -\frac{1}{4} (B^{-1})_{\alpha\beta} \right. \\
&\quad \times (r-r^c)_{\alpha} (r-r^c)_{\beta} \left. \right], \quad (10)
\end{aligned}$$

with the center of the packet (the first cumulant), denoted by  $\mathbf{r}^c$ , located at

$$r_z^c = G \sum_l A_l P_l(\cos \theta) [(l+1)f(g_l - g_{l+1}) + lf(g_l - g_{l-1})], \quad (11a)$$

$$\begin{aligned}
r_x^c &= G \sum_l A_l P_l^{(1)}(\cos \theta)(\cos \phi) \\
&\quad \times [f(g_l - g_{l-1}) - f(g_l - g_{l+1})], \quad (11b)
\end{aligned}$$

where  $G = c \exp(-\mu_a t)/F(s, s_0, t)$ ,  $A_l = (1/4\pi) \exp(-g_l t)$ ,  $g_l$  is defined after Eq. (4), and

$$f(g) = [\exp(gt) - 1]/g. \quad (12)$$

$r_y^c$  is obtained by replacing  $\cos \phi$  in Eq. (11b) by  $\sin \phi$ .

As an example, we derive Eq. (11a) as follows:

$$r_z^c = \frac{c}{F(s, s_0, t)} \int_0^t dt' \int ds' F(s, s', t-t') s'_z F(s', s_0, t'),$$

where  $F(s_2, s_1, t)$  is given by Eq. (4). We denote  $s = [s_x, s_y, s_z] = [\sin \theta \cos \phi, \sin \theta \sin \phi, \cos \theta]$ . The spherical harmonics addition theorem is given by [14]

$$\begin{aligned}
P_l(s_1, s_2) &= \sum_m \frac{\eta_m(l-m)!}{(l+m)!} P_l^{(m)}(\cos \theta_1) P_l^{(m)} \\
&\quad \times (\cos \theta_2) \cos[m(\phi_1 - \phi_2)], \quad (13)
\end{aligned}$$

where  $\eta_0 = 1$  and  $\eta_m = 2(m > 0)$ ,  $P_l^{(m)}(\cos \theta)$  is the associated Legendre function. The recurrence relations of the spherical harmonics is given by

$$\begin{aligned}
\cos \theta' P_l^{(m)}(\cos \theta') &= \frac{1}{2l+1} [(l-m+1) P_{l+1}^{(m)}(\cos \theta') \\
&\quad + (l+m) P_{l-1}^{(m)}(\cos \theta')]. \quad (14a)
\end{aligned}$$

$$\begin{aligned}
\sin \theta' P_l^{(m)}(\cos \theta') &= \frac{1}{2l+1} [P_{l+1}^{(m+1)}(\cos \theta') \\
&\quad - P_{l-1}^{(m+1)}(\cos \theta')]. \quad (14b)
\end{aligned}$$

The orthogonality relation of the spherical harmonics is

$$\begin{aligned}
& \int_{-1}^1 d \cos \theta' P_l^{(m)}(\cos \theta') P_{l'}^{(m)}(\cos \theta') \\
&= \frac{2}{2l+1} \frac{(l+m)!}{(l-m)!} \delta_{ll'}. \quad (15)
\end{aligned}$$

Using Eqs. (13)–(15) and making integrations, first over  $\phi'$ , then over  $\theta'$ , and last over  $t'$ , Eq. (11a) is obtained. Using a similar procedure, all results in this section were obtained.

The square of the average spread width (the second cumulant) is determined by

$$B_{\alpha\beta} = cG \Delta_{\alpha\beta} - r_\alpha^c r_\beta^c / 2, \quad (16)$$

with

$$\begin{aligned}
\Delta_{zz} &= \sum_l A_l P_l(\cos \theta) \left[ \frac{l(l-1)}{2l-1} E_l^{(1)} + \frac{(l+1)(l+2)}{2l+3} E_l^{(2)} \right. \\
&\quad \left. + \frac{l^2}{2l-1} E_l^{(3)} + \frac{(l+1)^2}{2l+3} E_l^{(4)} \right]. \quad (17a)
\end{aligned}$$

$$\begin{aligned}
\Delta_{xx,yy} &= \sum_l \frac{1}{2} A_l P_l(\cos \theta) \left[ -\frac{l(l-1)}{2l-1} E_l^{(1)} \right. \\
&\quad - \frac{(l+1)(l+2)}{2l+3} E_l^{(2)} + \frac{l(l-1)}{2l-1} E_l^{(3)} \\
&\quad \left. + \frac{(l+1)(l+2)}{2l+3} E_l^{(4)} \right] \pm \sum_l \frac{1}{2} A_l P_l^{(2)}(\cos \theta) \\
&\quad \times \cos(2\phi) \left[ \frac{1}{2l-1} E_l^{(1)} + \frac{1}{2l+3} E_l^{(2)} \right. \\
&\quad \left. - \frac{1}{2l-1} E_l^{(3)} - \frac{1}{2l+3} E_l^{(4)} \right], \quad (17b)
\end{aligned}$$

where (+) corresponds to  $\Delta_{xx}$  and (−) corresponds to  $\Delta_{yy}$ .

$$\Delta_{xy} = \Delta_{yx} = \sum_l \frac{1}{2} A_l P_l^{(2)}(\cos \theta) \sin(2\phi) \left[ \frac{1}{2l-1} E_l^{(1)} + \frac{1}{2l+3} E_l^{(2)} - \frac{1}{2l-1} E_l^{(3)} - \frac{1}{2l+3} E_l^{(4)} \right], \quad (17c)$$

$$\Delta_{xz} = \Delta_{zx} = \sum_l \frac{1}{2} A_l P_l^{(1)}(\cos \theta) (\cos \phi) \left[ \frac{2(l-1)}{2l-1} E_l^{(1)} - \frac{2(l+2)}{2l+3} E_l^{(2)} + \frac{1}{2l-1} E_l^{(3)} + \frac{1}{2l+3} E_l^{(4)} \right]. \quad (17d)$$

$\Delta_{yz}$  is obtained by replacing  $\cos \phi$  in Eq. (17d) by  $\sin \phi$ . In Eqs. (17a)–(17d)

$$E_l^{(1)} = [f(g_l - g_{l-2}) - f(g_l - g_{l-1})] / (g_{l-1} - g_{l-2}), \quad (18a)$$

$$E_l^{(2)} = [f(g_l - g_{l+2}) - f(g_l - g_{l+1})] / (g_{l+1} - g_{l+2}), \quad (18b)$$

$$E_l^{(3)} = [f(g_l - g_{l-1}) - t] / (g_l - g_{l-1}), \quad (18c)$$

$$E_l^{(4)} = [f(g_l - g_{l+1}) - t] / (g_l - g_{l+1}). \quad (18d)$$

A cumulant approximate expression for the photon density distribution is obtained from  $N(\mathbf{r}, t) = \langle \delta[\mathbf{r} - c \int_0^t \mathbf{s}(t') dt'] \rangle$ , where an average over the angular distribution is required. Using  $\int ds F(\mathbf{s}, \mathbf{s}', t) = \exp(-\mu_a t)$ , we have a Gaussian shape

$$N(\mathbf{r}, t) = \frac{1}{(4\pi D_{zz} ct)^{1/2}} \frac{1}{4\pi D_{xx} ct} \exp\left[-\frac{(z - R_z)^2}{4D_{zz} ct}\right] \times \exp\left[-\frac{(x^2 + y^2)}{4D_{xx} ct}\right] \exp(-\mu_a t), \quad (19)$$

with a moving center located at

$$R_z = c[1 - \exp(-g_1 t)] / g_1 \quad (20)$$

and the corresponding diffusion coefficients are given by

$$D_{zz} = \frac{c}{3t} \left\{ \frac{t}{g_1} - \frac{3g_1 - g_2}{g_1^2(g_1 - g_2)} [1 - \exp(-g_1 t)] + \frac{2}{g_2(g_1 - g_2)} [1 - \exp(-g_2 t)] - \frac{3}{2g_1^2} [1 - \exp(-g_1 t)]^2 \right\}, \quad (21a)$$

$$D_{xx} = D_{yy} = \frac{c}{3t} \left\{ \frac{t}{g_1} + \frac{g_2}{g_1^2(g_1 - g_2)} [1 - \exp(-g_1 t)] - \frac{1}{g_2(g_1 - g_2)} [1 - \exp(-g_2 t)] \right\}. \quad (21b)$$

In contrast to Eqs. (11) and (17), these results are independent of  $g_l$  for  $l > 2$ . Figure 1 shows the moving center of photons,  $R_z$  [Eq. (20)], and the diffusion coefficients,  $D_{zz}$  and  $D_{xx}$  [Eqs. (21)], as function of time, where  $g_l$  are calcu-

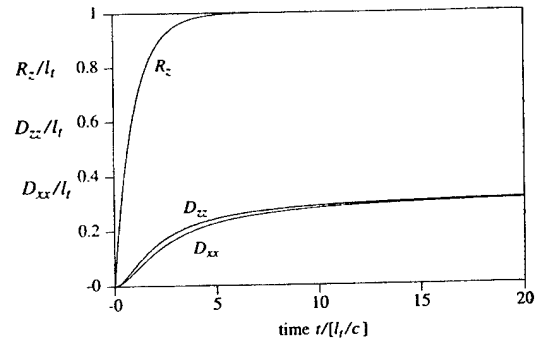


FIG. 1. The moving center of photon density function  $R_z$  [Eq. (20)] and the diffusion coefficients  $D_{zz}$  and  $D_{xx}$  [Eqs. (21)], as a function of time  $t$ .

lated by Mie theory [10] assuming (for this figure) water droplets with  $r/\lambda = 1$  are uniformly distributed in air, with  $r$  the radius of the droplet,  $\lambda$  the wavelength of light, and the index of refraction  $m = 1.33$ .

Each distribution in Eq. (10) and Eq. (19) describes a photon "cloud" anisotropically spreading from a moving center, with time-dependent diffusion coefficients. At early time  $t \rightarrow 0$ ,  $f(g) \approx t + O(t^2)$  in Eq. (12), and  $E_l^{(j)} = t^2/2 + O(t^3)$  for  $j = 1, 2, 3, 4$  in Eqs. (18). From Eqs. (11), Eqs. (17), and Eqs. (20) and (21), we see that for the density distribution,  $N(\mathbf{r}, t)$ , and the dominant distribution function, that is  $I(\mathbf{r}, \mathbf{s}, t)$  along  $\mathbf{s} = \mathbf{s}_0$ , the center moves as  $ct \mathbf{s}_0$  and the  $B_{\alpha\beta}$  in Eq. (16) are proportional to  $t^3$  at  $t \rightarrow 0$ . A distribution function  $I(\mathbf{r}, \mathbf{s}, t)$  along  $\mathbf{s} \neq \mathbf{s}_0$  is small since  $F(\mathbf{s}, \mathbf{s}_0, t) \sim t$  when  $t \rightarrow 0$ . Its center moves at a certain direction with displacement proportional to  $ct$ , and the  $B_{\alpha\beta}$  in Eq. (16) are proportional to  $t^2$  at  $t \rightarrow 0$ . These results present a clear picture of nearly ballistic motion at  $t \rightarrow 0$ . Roughly speaking, this near ballistic motion maintains its speed up to  $R_z \approx 0.6l_i$  [see Eq. (20)]. This closely agrees with experimental results of optical coherent tomography (OCT) [15] that the range of good resolution extends to about  $600 \mu\text{m}$ , in a tissue of  $l_i \sim 1 \text{ mm}$ . With increase of time, the motion of the center slows down, and the diffusion coefficients increase from zero. This stage of photon migration is often called a "snakelike mode."

With further increase in time, the  $l$ th Legendre component in Eqs. (4), (11), and (17), exponentially decay with a rate related to  $g_l$ . The detailed decay rate,  $g_l$ , is determined by the shape of the phase function. Generally speaking, the very high  $l$ th components decays in a rate of order of  $\mu_s$ , as long as its Legendre coefficient  $a_l$  distinctly smaller than  $2l + 1$ . Even in the case that the phase function has a very sharp forward peak, in which there are nonzero  $a_l$  for very high  $l$ th rank, the  $a_l$  are, usually, much smaller than  $2l + 1$ . Therefore, for the distribution function at time  $t$  after the ballistic stage is over, a truncation in the summation over  $l$  is available.

At large times, the distribution function tends to become isotropic. From Eqs. (19)–(21), the photon density, at  $t \gg l_i/c$  and  $r \gg l_i$ , tends towards the conventional diffusion solution with the diffusive coefficient  $l_i/3$ . Therefore, our solution quantitatively describes how the photon migrates from nearly ballistic motion to diffusive motion.

#### IV. COMPARISON WITH AN EXACT SOLUTION IN THE ISOTROPIC SCATTERING CASE

A check of our angular distribution, Eq. (4), the first moments, Eq. (11), and the second moments, Eq. (17), for a special case of isotropic scattering is performed by comparing with the exact solution given by Hauge [9] and agreement is verified. Hauge has provided an exact solution for isotropic scattering in the form of a Fourier transform in space and Laplace transform in time, which is given by

$$I_{k\zeta}(s) \equiv \int_0^\infty dt e^{-\zeta t} \int d\mathbf{r} e^{-i\mathbf{k} \cdot \mathbf{r}} I(\mathbf{r}, s, t), \quad (22)$$

with

$$I_{k\zeta}(s) = \frac{\mu}{\zeta + \mu + i\mathbf{k} \cdot c\mathbf{s}_0} \left[ 1 - \frac{\mu}{|\mathbf{k}|c} \tan^{-1} \frac{|\mathbf{k}|c}{\zeta + \mu} \right]^{-1} \times \frac{1}{4\pi} \frac{1}{\zeta + \mu + i\mathbf{k} \cdot c\mathbf{s}_0} + \frac{\delta(s-s_0)}{\zeta + \mu + i\mathbf{k} \cdot c\mathbf{s}_0}. \quad (23)$$

In order to compare, we set  $\mu_a = 0$  and  $\mu_s \equiv \mu$  in this paper. In the case of isotropic scattering,  $g_0 = 0$ , and  $g_l = \mu$ ,  $l = 1, 2, \dots$

Equation (4) in the isotropic scattering case, reduces to

$$F(s, s_0, t) = \frac{1}{4\pi} [1 - e^{-\mu t}] + e^{-\mu t} \delta(s - s_0). \quad (24)$$

Its Laplace transform in time is given by

$$\mathcal{L}[F(s, s_0, \zeta)] = \frac{1}{4\pi} \frac{\mu}{\zeta(\zeta + \mu)} + \frac{\delta(s - s_0)}{\zeta + \mu}. \quad (25)$$

If Eq. (23) is evaluated at  $\mathbf{k} = 0$ , that means integration of  $I(\mathbf{r}, s, t)$  over  $\mathbf{r}$ , the result is the same as Eq. (25). Thus the exactness of  $F(s, s_0, t)$  is verified for the isotropic scattering case.

The first moments, Eqs. (11), without normalization, [without divided by  $F(s, s_0, t)$ ], for the isotropic scattering case, reduce by our procedure to

$$\bar{r}_z^c = c \left[ \frac{1 + \cos \theta}{4\pi} \left( \frac{1 - e^{-\mu t}}{\mu} - t e^{-\mu t} \right) + t e^{-\mu t} \delta(s - s_0) \right]. \quad (26a)$$

$$\bar{r}_x^c = c \sin \theta \cos \phi \frac{1}{4\pi} \left[ \frac{1 - e^{-\mu t}}{\mu} - t e^{-\mu t} \right]. \quad (26b)$$

These coordinates of the center have the Laplace transforms, given by

$$\mathcal{L}[\bar{r}_z^c] = c \left[ \frac{1 + \cos \theta}{4\pi} \frac{\mu}{\zeta(\zeta + \mu)^2} + \frac{\delta(s - s_0)}{(\zeta + \mu)^2} \right], \quad (27a)$$

$$\mathcal{L}[\bar{r}_x^c] = c(\sin \theta)(\cos \phi) \frac{1}{4\pi} \frac{\mu}{\zeta(\zeta + \mu)^2}. \quad (27b)$$

Since moments can be obtained by differentiation of characteristic functions, we evaluate  $\partial/\partial(-ik_\alpha)\{Eq.(23)\}|_{\mathbf{k}=0}$ , that means integration over space of  $r_\alpha$  with  $I(\mathbf{r}, s, t)$  as

weight. The results are same as Eqs. (27). Thus, by a slight extension of Hauge's results we verify the exactness of our first moment in the isotropic scattering case.

For a check of the second moment, we notice that Eqs. (18) are obtained from

$$\int_0^t dt' \exp(at') \int_0^{t'} dt'' \exp(bt'') = \begin{cases} (1/b)[(e^{(a+b)t} - 1)/(a+b) - (e^{at} - 1)/a], \\ (1/a)[(e^{at} - 1)/a - t], & a = -b. \end{cases} \quad (28)$$

In the isotropic scattering case, the limit as  $a \rightarrow 0$ , or  $b \rightarrow 0$ , or both is needed.

Equation (17a), without normalization, in the isotropic scattering case reduce to

$$\bar{\Delta}_{zz}^c = c^2 \frac{\cos^2 \theta + \cos \theta}{4\pi} \left[ \frac{1}{\mu^2} - e^{-\mu t} \frac{1}{\mu^2} - e^{-\mu t} \frac{t}{\mu} - e^{-\mu t} \frac{t^2}{2} \right] + \frac{c^2}{12\pi} \left[ \frac{t}{\mu} - e^{-\mu t} \frac{t}{\mu} - e^{-\mu t} t^2 \right] + c^2 \frac{t^2}{2} e^{-\mu t} \delta(s - s_0). \quad (29)$$

This moment based on our method has a Laplace transform, given by

$$\mathcal{L}[\bar{\Delta}_{zz}^c] = c^2 \frac{\cos^2 \theta + \cos \theta}{4\pi} \frac{\mu}{\zeta(\zeta + \mu)^3} + \frac{c^2}{12\pi} \frac{\mu^2 + 3\zeta\mu}{\zeta^2(\zeta + \mu)^3} + \frac{c^2}{(\zeta + \mu)^3} \delta(s - s_0). \quad (30)$$

The corresponding result from Hauge's solution are obtained by  $(1/2)\partial^2/\partial(-ik_z)\partial(-ik_z)\{Eq.(23)\}|_{\mathbf{k}=0}$ , which implies integration of  $(r_z r_z)/2$  with  $I(\mathbf{r}, s, t)$  as weight over space. The same result as Eq. (30) is obtained. The similar proofs have been performed for  $\bar{\Delta}_{xx}^c$ ,  $\bar{\Delta}_{yy}^c$ ,  $\bar{\Delta}_{xz}^c$ ,  $\bar{\Delta}_{yz}^c$ , and  $\bar{\Delta}_{xy}^c$ , verifying the exactness of our second moments. In evaluation of the value and the derivatives of  $B \equiv \{1 - (\mu/|\mathbf{k}|c) \tan^{-1} [|\mathbf{k}|c/(\zeta + \mu)]\}^{-1}$  at  $\mathbf{k} = 0$ , we have  $B = (\zeta + \mu)/\zeta$ ,  $B_\alpha = 0$ ,  $B_{\alpha\alpha} = 2\mu c^2/[3\zeta^2(\zeta + \mu)]$ , and  $B_{\alpha\beta} = 0$  if  $\alpha \neq \beta$ .

In the above equations the term related to  $e^{-\mu t} \delta(s - s_0)$ , has cumulants  $r_z^c = ct$  and  $2\bar{\Delta}_{zz} - (r_z^c)^2 = 0$ . This spike represents the unscattered part of the light, which reduces its intensity as  $\exp(-\mu t)$ . The scattered part of light along the directions of  $\mathbf{s} \neq \mathbf{s}_0$  has the correct mean positions and spreads, as has been proved.

#### V. DISCUSSION

The decoupling of harmonics is valid only for the angular distribution,  $F(s, s_0, t)$ , because in Eq. (3) the term such as  $c\mathbf{s} \cdot \nabla I(\mathbf{r}, s, t)$  in Eq. (1) disappears. This result is available only for an infinite uniform medium, otherwise Eq. (3) cannot be derived from Eq. (1). When the spatial related distribution,  $I(\mathbf{r}, s, t)$ , is calculated, the coupling of the different harmonics remains, and is presented in Eqs. (8) and (9), through the recurrence relation of harmonics, Eq. (14), and

explicitly shown in Eqs. (11) and (17), the results of the first two moments. Contrasting with the usual approach using angular moment expansion of Eq. (1), our cumulant approach has two remarkable features: (a) since the formula for calculating cumulants, Eqs. (8) and (9) (and possible extension to higher order cumulants), use the standard Green's function approach without making approximation and the Green's function, Eq. (4), is exact, the obtained cumulants, as far as the  $n$ th order concern, are exact. (b) The cumulants obtained appear as the arguments of the exponential functions in Eq. (7), that implies that an infinite series in the usual angular moment expansion has been included. Therefore, even though only derived by terminating at the second order cumulant, the distribution function obtained has the exact central position and the exact half-width as functions of time, and thus leads to the correct ballistic limit at  $t \rightarrow 0$  and correct diffusive limit at large  $t$ . This result is not achieved for a general phase function in any known publication.

The cumulant expansion terminating at the second order is a standard method in statistics [12], which neglects all cumulants higher than second order, and leads to a Gaussian distribution. If we examine the spatial displacement after each collision event as an independent random variable,  $\Delta \mathbf{r}_i$ , the total displacement is  $\sum \Delta \mathbf{r}_i (i=1, \dots, N)$ . The central limit theorem claims that if  $N$  is a large number, then the sum of  $N$  variables will have an essentially Gaussian distribution. Therefore, after enough collision events happened, the distributions we calculated become accurate in detail, not just having the correct center and spread. At early time, the pho-

ton spread is narrow, hence, in many applications the detailed shape is less important than the correct position and correct narrow width of the beam.

In case a more accurate distribution at early time is needed, the exact higher (than second) order cumulants can be analytically calculated, and Eq. (7) can be extended to higher order. Analytical expressions for exact spatial cumulants up to an arbitrary  $n$ th high order have been derived, and will be presented elsewhere [16]. However, a closed analytical form in space is unlikely to result, and a numerical Fourier transform over  $\mathbf{k}$  would be required. We have therefore terminated the current calculation at second order in this paper.

In summary, we have derived an analytical solution of the distribution function, Eq. (10), and the density distribution, Eq. (19), for the elastic Boltzmann transport equation in an infinite uniform medium. This solution is quantitatively accurate up to the second order cumulant approximation and shows a clear picture of time evolution of particle migration from ballistic to snakelike, then to the diffusion regime. The first two position cumulants at any angle and the angular distribution are completely exact as functions of time.

#### ACKNOWLEDGMENTS

This work was supported in part by NASA, U.S. DOE, ARO, and the New York State Science, and Technology Foundation.

- 
- [1] K. M. Case and P. F. Zweifel, *Linear Transport Theory* (Addison-Wesley, New York, 1967), and references therein.
  - [2] J. J. Duderstadt and W. R. Martin, *Transport Theory* (Wiley, New York, 1979), and references therein.
  - [3] S. Chandrasekhar, *Radiative Transfer* (Oxford University Press, Oxford, 1950), and references therein.
  - [4] S. R. Arridge, *Appl. Opt.* **34**, 7395 (1995).
  - [5] I. Ishimaru, *Appl. Opt.* **28**, 2210 (1989).
  - [6] A. Ya Polishchuk and R. R. Alfano, *Opt. Lett.* **21**, 916 (1996).
  - [7] L. T. Perelman, J. Wu, I. Itzkan, and M. S. Feld, *Phys. Rev. Lett.* **72**, 1341 (1994).
  - [8] A. Ishimaru, *Wave Propagation and Scattering in Random Media* (Academic, London, 1978), Vol. 2, pp. 296–301.
  - [9] E. H. Hauge, in *Transport Phenomena*, edited by G. Kirczenow and J. Marro (Springer-Verlag, Berlin, 1974), pp. 337–367.
  - [10] C. F. Bohren and D. R. Huffman, *Absorption and Scattering of light by Small Particles* (Wiley, New York, 1983).
  - [11] See, for example, M. Lax, *Rev. Mod. Phys.* **32**, 25 (1960).
  - [12] Nelson Wax, *Selected Papers on Noise and Stochastic Processes* (Dover, New York, 1954); S. K. Ma, *Statistical Mechanics* (World Scientific, Philadelphia, 1985), pp. 198–211.
  - [13] R. P. Feynman, *Phys. Rev.* **84**, 108 (1951); F. Dyson, *ibid.* **75**, 486 (1949).
  - [14] P. M. Morse and H. Feshbach, *Method of Theoretical Physics* (McGraw-Hill, New York, 1953), Pt. 2, pp. 1325–1330.
  - [15] D. Huang, E. A. Swanson, C. P. Lin, J. S. Schuman, W. G. Stinson, W. Chang, M. R. Hee, T. Flotte, K. Gregory, C. A. Puliafito, and J. G. Fujimoto, *Science* **254**, 1178 (1991).
  - [16] W. Cai, M. Lax, and R. R. Alfano, *J. Phys. Chem.* (to be published).

# Appendix 4

Accepted for publication in *Journal of Optical Society of America A*

## Time-resolved optical diffuse tomography

M. Xu, M. Lax, R. R. Alfano

Institute for Ultrafast Spectroscopy and Lasers, New York State

Center of Advanced Technology for Ultrafast Photonic

Materials and Applications, and Department of Physics,

The City College and Graduate Center of City University of

New York, New York, NY 10031

*minxu@sci.ccny.cuny.edu*

Time-resolved Fourier optical diffuse tomography is a novel approach for imaging of objects in a highly scattering turbid medium using an incident (near) plane wave. The theory of the propagation of spatial Fourier components of the scattered wave field is presented, with a fast algorithm for three-dimensional reconstruction in a parallel planar geometry. An example of successful reconstruction of four simulated hidden absorptive objects up to 2cm below the surface inside a human tissue like semi-infinite turbid medium is provided at the end. ©2000 Optical Society of America

OCIS codes: 170.6960, 290.7050, 290.1350

## 1. Introduction

Research on near-infrared (NIR) diffusive light for biomedical imaging and diagnosis has advanced over the past decade because of its potential to be a safe, non-invasive, affordable and superior diagnostics.<sup>1-3</sup> To seek a methodology which provides fast data acquisition and reconstruction to perform imaging with high resolution in real time, a variety of techniques have been explored including time resolved picosecond pulses, continuous waves, and diffuse photon density waves (DPDW). Most methods reconstruct three-dimensional optical property maps (OPM) by a matrix inversion or iterative techniques, or by three-dimensional rendering of two dimensional projection images.<sup>4-8</sup> The difficulty of inverting the whole three-dimensional map at once is usually time prohibitive when the number of volume elements involved increases, while three-dimensional rendering of two dimensional projection images needs extra depth information of inhomogeneities inside turbid media to behave well and has other limitations.<sup>7,9</sup>

In this article, we introduce the theory of propagation of the spatial Fourier component of the scattered wave field inside the turbid medium, and then develop a new optical diffuse imaging methodology based on this theory, using the two-dimensional Fourier transform of photon intensity on a plane to detect inhomogeneities in a highly scattering turbid medium when illuminated by a picosecond (near) plane wave pulse. In such a spatial Fourier space, the picture of photon migration is much simplified, in the sense that different spatial frequency components of the OPM (2D Fourier transform on the  $xy$  plane) are decoupled from each other and only depend on the corresponding spatial frequency component of the photon intensity on the detector plane. Based on this observation, we obtain a super-fast reconstruction of 3D OPM by matrix inversions of each spatial component independently. The effect of noise is explicitly handled by controlling the set of spatial frequency components and the regularization parameters used in the matrix inversion. After a rigorous account of the theory and a brief description of the algorithm, an example of

reconstruction of four inhomogeneities located up to 2cm below the surface of a human tissue like semi-infinite turbid medium using backscattered photons is presented at the end.

## 2. Theory

The photon density  $\phi(\mathbf{r}, t)$  at position  $\mathbf{r}$  and time  $t$  in a highly scattering turbid medium can be described by the diffusion equation

$$\frac{\partial}{\partial t}\phi(\mathbf{r}, t) - c\nabla \cdot D(\mathbf{r})\nabla\phi(\mathbf{r}, t) + c\mu_a(\mathbf{r})\phi(\mathbf{r}, t) = S(\mathbf{r}, t) \quad (1)$$

The absorption coefficient  $\mu_a$ , and the diffusion coefficient  $D = 1/3\mu'_s$  where  $\mu'_s$  is the reduced scattering coefficient, may depend on the position in the medium.  $c$  is the speed of light inside the medium, and  $S$  is the source term describing the density of photons generated per second.

For the case of a uniform medium and an incident source  $S(\mathbf{r}, t)$  ( $S = 0$  when  $t < 0$ ), the incident wave field is  $\phi_i(\mathbf{r}, t) = \int d^3\mathbf{r}' \int_0^t dt' S(\mathbf{r}', t') G(\mathbf{r}, \mathbf{r}', t - t')$  where  $G(\mathbf{r}, \mathbf{r}', t)$  is the Green's function for the diffusion equation in a uniform turbid medium. When some weak inhomogeneities (objects such as tumors) are embedded in the medium, we write:

$$\begin{aligned} \mu_{a,\text{obj}}(\mathbf{r}) &= \mu_a + \delta\mu_a(\mathbf{r}) \\ \mu'_{s,\text{obj}}(\mathbf{r}) &= \mu'_s + \delta\mu'_s(\mathbf{r}) \end{aligned} \quad (2)$$

where  $\mu_a$  and  $\mu'_s$  are the constant absorption and the reduced scattering coefficients of the otherwise homogeneous medium,  $\mu_{a,\text{obj}}(\mathbf{r})$  and  $\mu'_{s,\text{obj}}(\mathbf{r})$  are the absorption and the reduced scattering coefficients of the embedded inhomogeneity which are spatially dependent. Plug Eq. (2) into Eq. (1), and note the diffusion parameter of the inhomogeneity  $D_{\text{obj}}(\mathbf{r}) = D + \delta D(\mathbf{r}) = 1/3\mu'_s - \delta\mu'_s(\mathbf{r})/3\mu_s'^2$ , we have

$$\frac{\partial}{\partial t}\phi(\mathbf{r}, t) - Dc\nabla^2\phi(\mathbf{r}, t) + \mu_a c\phi(\mathbf{r}, t) = S(\mathbf{r}, t) + c\nabla \cdot \delta D(\mathbf{r})\nabla\phi(\mathbf{r}, t) - c\delta\mu_a(\mathbf{r})\phi(\mathbf{r}, t) \quad (3)$$

The complete right-hand side of Eq. (3) now acts as the source term, of which,  $S(\mathbf{r}, t)$  contributes to the unperturbed wave field  $\phi_0 = \phi_i(\mathbf{r}, t)$ , and the rest contributes to the scattered wave field,

$$\begin{aligned}
\phi_s(\mathbf{r}, t) &= \phi(\mathbf{r}, t) - \phi_0(\mathbf{r}, t) \\
&= \int d^3\mathbf{r}' \int_0^t dt' G(\mathbf{r}, \mathbf{r}', t - t') (c \nabla_{\mathbf{r}'} \cdot \delta D(\mathbf{r}') \nabla_{\mathbf{r}'} \phi(\mathbf{r}', t') - c \delta \mu_a(\mathbf{r}') \phi(\mathbf{r}', t')) \\
&= - \int d^3\mathbf{r}' \int_0^t dt' G(\mathbf{r}, \mathbf{r}', t - t') \delta \mu_a(\mathbf{r}') c \phi(\mathbf{r}', t') \\
&\quad + \int d^3\mathbf{r}' \int_0^t dt' \frac{\delta \mu'_s(\mathbf{r}') c}{3\mu_s'^2} \nabla_{\mathbf{r}'} G(\mathbf{r}, \mathbf{r}', t - t') \cdot \nabla_{\mathbf{r}'} \phi(\mathbf{r}', t')
\end{aligned} \tag{4}$$

after partial integration.

To the first order in the variation of optical absorption and reduced scattering coefficients, we can just replace  $\phi(\mathbf{r}', t')$  in Eq. (4) by  $\phi_i$ , i.e., the total wave field is a superposition of the incident wave field  $\phi_i$  and the singly scattered wave field  $\phi_s$ . This is the well-known Born approximation.

Now consider the configuration of mostly studied parallel planar geometry with its boundaries at  $z = 0$  and  $z = d$ . Its Green function is thus<sup>10</sup>

$$G(\mathbf{r}, \mathbf{r}', t) = \frac{1}{4\pi Dct} \exp\left(-\frac{|\rho - \rho'|^2}{4Dct} - \mu_a ct\right) G_z(z, z', t), \quad (t > 0) \tag{5}$$

where  $\rho = (x, y)$ ,  $\rho' = (x', y')$ , and  $G_z(z, z', t)$  can be easily obtained by an image method. Its two dimensional Fourier transform on  $\rho$ ,

$$\begin{aligned}
\hat{G}(\mathbf{q}, z, \rho', z', t) &= \int d^2\rho G(\rho, z, \rho', z', t) \exp(-i\mathbf{q} \cdot \rho) \\
&= \exp(-i\mathbf{q} \cdot \rho' - Dctq^2 - \mu_a ct) G_z(z, z', t) \\
&= \hat{G}(\mathbf{q}, z, z', t) \exp(-i\mathbf{q} \cdot \rho')
\end{aligned} \tag{6}$$

For simplicity, let's restrict ourselves to the case of a pure absorptive perturbation ( $\delta\mu_a \neq 0$  and  $\delta\mu'_s = 0$ ) and of an incident pulse  $S(\mathbf{r}, t) = S(\rho)\delta(z - z_s)\delta(t)$  at this moment. The scattered

wave field on a plane  $0 < z < d$  is thus

$$\phi_s(\rho, z, t) = - \int d^3\mathbf{r}' \int d^2\rho'' \int_0^t dt' G(\mathbf{r}, \mathbf{r}', t - t') \delta\mu_a(\mathbf{r}') cS(\rho'') G(\mathbf{r}', \rho'', z_s, t'). \quad (7)$$

from Eq. (4) after replacing  $\phi$  by  $\phi_i$ . Inside Eq. (7), expand the source term  $S(\rho'')$ , and Green functions  $G(\mathbf{r}, \mathbf{r}', t - t')$  and  $G(\mathbf{r}', \rho'', z_s, t')$  into integrals of their Fourier components, we find:

$$\begin{aligned} \phi_s(\rho, z, t) &= -\frac{1}{(4\pi^2)^3} \int d^2\rho' \int dz' \int d^2\rho'' \int_0^t dt' \int d^2\mathbf{q} \hat{G}(\mathbf{q}, z, z', t - t') \exp(i\mathbf{q} \cdot (\rho - \rho')) \\ &\quad \times \delta\mu_a(\rho', z') c \int d^2\mathbf{q}'' S(\mathbf{q}'') \exp(i\mathbf{q}'' \cdot \rho'') \int d^2\mathbf{q}' \hat{G}(\mathbf{q}', z', z_s, t') \exp(i\mathbf{q}' \cdot (\rho' - \rho'')) \\ &= -\frac{c}{(4\pi^2)^3} \int d^2\mathbf{q} \int d^2\mathbf{q}' \int d^2\mathbf{q}'' \int_0^t dt' \int dz' \exp(i\mathbf{q} \cdot \rho) \hat{G}(\mathbf{q}, z, z', t - t') S(\mathbf{q}'') \hat{G}(\mathbf{q}', z', z_s, t') \\ &\quad \times \int d^2\rho' \delta\mu_a(\rho', z') \exp(-i\rho' \cdot (\mathbf{q} - \mathbf{q}')) \int d^2\rho'' \exp(i\rho'' \cdot (\mathbf{q}'' - \mathbf{q}')) \\ &= -\frac{c}{(4\pi^2)^2} \int d^2\mathbf{q} \int d^2\mathbf{q}' \int_0^t dt' \int dz' \exp(i\mathbf{q} \cdot \rho) \hat{G}(\mathbf{q}, z, z', t - t') \delta\hat{\mu}_a(\mathbf{q} - \mathbf{q}', z') \\ &\quad \times S(\mathbf{q}') \hat{G}(\mathbf{q}', z', z_s, t') \end{aligned} \quad (8)$$

where  $\hat{S}(\mathbf{q}, z_s)$ ,  $\delta\hat{\mu}_a(\mathbf{q}, z)$  are two-dimensional Fourier transforms of the source on the  $z = z_s$  plane, and of the perturbation of absorption coefficient over the  $z = z$  plane, respectively. And at last, we recognize the two dimensional Fourier transform of the scattered wave field  $\phi_s(\rho, z, t)$  on a plane  $z$  for the case of a pure absorptive perturbation

$$\hat{\phi}_s(\mathbf{q}, z, t) = -\frac{c}{4\pi^2} \int d^2\mathbf{q}' dz' \delta\hat{\mu}_a(\mathbf{q} - \mathbf{q}', z') \hat{S}(\mathbf{q}', z_s) \int_0^t dt' \hat{G}(\mathbf{q}, z, z', t - t') \hat{G}(\mathbf{q}', z', z_s, t') \quad (9)$$

In a similar fashion, for the case of a pure scattering perturbation ( $\delta\mu_a = 0$  and  $\delta\mu'_s \neq 0$ ), the two-dimensional Fourier transform of the scattered wave field is:

$$\begin{aligned} \hat{\phi}_s(\mathbf{q}, z, t) &= \frac{c}{12\pi^2 \mu_s'^2} \int d^2\mathbf{q}' dz' \delta\hat{\mu}'_s(\mathbf{q} - \mathbf{q}', z') \hat{S}(\mathbf{q}', z_s) \\ &\quad \times \int_0^t dt' \{ \mathbf{q} \cdot \mathbf{q}' \hat{G}(\mathbf{q}, z, z', t - t') \hat{G}(\mathbf{q}', z', z_s, t') \\ &\quad + \frac{\partial \hat{G}(\mathbf{q}, z, z', t - t')}{\partial z'} \frac{\partial \hat{G}(\mathbf{q}', z', z_s, t')}{\partial z'} \} \end{aligned} \quad (10)$$

The general Fourier scattered wave field is the sum of Eq. (9) and Eq. (10). Denote the convolutions

$$\begin{aligned} w_a(\mathbf{q}, \mathbf{q}', z, t; z') &= \int_0^t dt' \hat{G}(\mathbf{q}, z, z', t - t') \hat{G}(\mathbf{q}', z', z_s, t') \\ w_s(\mathbf{q}, \mathbf{q}', z, t; z') &= \int_0^t dt' \frac{\partial \hat{G}(\mathbf{q}, z, z', t - t')}{\partial z'} \frac{\partial \hat{G}(\mathbf{q}', z', z_s, t')}{\partial z'} \end{aligned} \quad (11)$$

which are the weight functions involved in the propagation of spatial Fourier components of the scattered wave field, we have

$$\begin{aligned} \hat{\phi}_s(\mathbf{q}, z, t) &= -\frac{c}{4\pi^2} \int d^2 \mathbf{q}' dz' \delta \hat{\mu}_a(\mathbf{q} - \mathbf{q}', z') \hat{S}(\mathbf{q}', z_s) w_a(\mathbf{q}, \mathbf{q}', z, t; z') \\ &\quad + \frac{c}{12\pi^2 \mu_s'^2} \int d^2 \mathbf{q}' dz' \delta \hat{\mu}_s'(\mathbf{q} - \mathbf{q}', z') \hat{S}(\mathbf{q}', z_s) \\ &\quad \times \{ \mathbf{q} \cdot \mathbf{q}' w_a(\mathbf{q}, \mathbf{q}', z, t; z') + w_s(\mathbf{q}, \mathbf{q}', z, t; z') \} \end{aligned} \quad (12)$$

#### A. Incident plane wave

For the simple case when the incident wave is a plane wave pulse, i.e.,  $S(\mathbf{r}, t) = S\delta(z - z_s)\delta(t)$ , such that  $\hat{S}(\mathbf{q}, z_s) = 4\pi^2 S\delta(\mathbf{q})$ , Eq. (12) simplifies to:

$$\hat{\phi}_s(\mathbf{q}, z, t) = -Sc \int dz' \{ \delta \hat{\mu}_a(\mathbf{q}, z') w_a(\mathbf{q}, 0, z, t; z') - \frac{\delta \hat{\mu}_s'(\mathbf{q}, z')}{3\mu_s'^2} w_s(\mathbf{q}, 0, z, t; z') \} \quad (13)$$

The most salient feature of the above result is that different spatial frequency components of  $\delta \hat{\mu}_a$  and  $\delta \hat{\mu}_s'$  are decoupled from each other and the  $\mathbf{q}$ -component of the optical parameters depends only on the corresponding spatial frequency component of the scattered wave field. Thus the dimension of the inverse problem to be solved later is greatly reduced, as is the computation time.

Let's approximate the integration over  $z'$  by a summation, and fix  $z = z_d$  at the detection plane (omit  $z$  hereafter), the Fourier scattered wave field on the detection plane

$$\hat{\phi}_s(\mathbf{q}, t) = Sc\Delta z \sum_{j=1}^N [-\delta \hat{\mu}_a(\mathbf{q}, z_j) w_a(\mathbf{q}, 0, t; z_j) + \frac{\delta \hat{\mu}_s'(\mathbf{q}, z_j)}{3\mu_s'^2} w_s(\mathbf{q}, 0, t; z_j)] \quad (14)$$

where  $\Delta z$  is the discretized step size,  $N$  is the total number of slices (layers) in the  $z$  direction between the source plane and detection plane, and  $z_j$  is the  $z$ -coordinate of the central position of layer  $j$ .

Set  $\mathbf{q} = 0$  in Eq. (14),

$$\hat{\phi}_s(0, t) = Sc\Delta z \sum_{j=1}^N [-\delta\hat{\mu}_a(0, z_j)w_a(0, 0, t; z_j) + \frac{\delta\hat{\mu}'_s(0, z_j)}{3\mu_s'^2}w_s(0, 0, t; z_j)], \quad (15)$$

the zero spatial frequency components  $\delta\hat{\mu}_a(0, z_j)$  and  $\delta\hat{\mu}'_s(0, z_j)$  can be readily solved without doing a complete reconstruction. Due to the nature of Fourier transform, they just provide the profile of the amount of total perturbation of absorption and reduced scattering coefficients per slice, i.e., the depth profile of the inhomogeneities.

The whole three-dimensional absorption and reduced scattering coefficients map is thus constructed through an inverse Fourier transform from all the  $\mathbf{q}$ -components of  $\delta\hat{\mu}_a$  and  $\delta\hat{\mu}'_s$  at different depths, each of which is solved independently from a series of time resolved scattered wave field  $\hat{\phi}_s$  by Eq. (14). A schematic diagram of the procedure of inversion is shown in Fig. (1). The maximum spatial frequency (cutoff frequency) of the components used in the inversion is determined through a signal-noise-ratio analysis and the regularization parameter in the matrix inversion is obtained by the robust L-curve method.<sup>11</sup>

Both transmission and/or backscattering image reconstruction configurations can easily be made using Eqs. (13) and (14).

## B. Near plane wave

When the incident wave is not a perfect plane wave but nearly plane, we write  $S(\mathbf{r}, t) = (S + \Delta S(\rho))\delta(z - z_s)\delta(t)$  where  $S$  is the mean value of  $S(\mathbf{r}, t)$  on the  $z = z_s$  plane, and

$$\hat{S}(\mathbf{q}, z_s) = 4\pi^2 S(\delta(\mathbf{q}) + f(\mathbf{q})) \quad (16)$$

where  $f(\mathbf{q}) \ll 1$  and  $f(0) = 0$ . Regard  $4\pi^2 S f(\mathbf{q})$  as a perturbation to  $\hat{S}^{(0)} = 4\pi^2 S \delta(\mathbf{q})$ , producing extra deviations in  $\delta\hat{\mu}_a$  and  $\delta\hat{\mu}'_s$  such that

$$\begin{aligned}\delta\hat{\mu}_a(\mathbf{q}, z) &= \delta\hat{\mu}_a^{(0)}(\mathbf{q}, z) + \varepsilon_a(\mathbf{q}, z) \\ \delta\hat{\mu}_s(\mathbf{q}, z) &= \delta\hat{\mu}_s^{(0)}(\mathbf{q}, z) + \varepsilon_s(\mathbf{q}, z)\end{aligned}\tag{17}$$

where  $\delta\hat{\mu}_a^{(0)}(\mathbf{q}, z)$  and  $\delta\hat{\mu}_s^{(0)}(\mathbf{q}, z)$  are the solution of Eq. (13) with the same scattered wave field on the detection plane  $z = z_d$  for a perfect plane wave source  $\hat{S}^{(0)}$ . Plug Eqs. (17) into Eq. (12), after rearranging the terms and retaining only up to the first order of perturbation  $f(\mathbf{q})$ , we get:

$$\begin{aligned}& -Sc \int dz' \{ \varepsilon_a(\mathbf{q}, z') w_a(\mathbf{q}, 0, z, t; z') - \frac{\varepsilon_b(\mathbf{q}, z')}{3\mu_s'^2} w_s(\mathbf{q}, 0, z, t; z') \} \\ &= Sc \int d^2\mathbf{q}' dz' f(\mathbf{q}') w_a(\mathbf{q}, \mathbf{q}', z, t; z') \{ \delta\hat{\mu}_a^{(0)}(\mathbf{q} - \mathbf{q}', z') - \frac{\mathbf{q} \cdot \mathbf{q}' \delta\hat{\mu}_s^{(0)}(\mathbf{q} - \mathbf{q}', z')}{3\mu_s'^2} \} \\ & - Sc \int d^2\mathbf{q}' dz' f(\mathbf{q}') w_s(\mathbf{q}, \mathbf{q}', z, t; z') \delta\hat{\mu}_s^{(0)}(\mathbf{q} - \mathbf{q}', z')\end{aligned}\tag{18}$$

Please note, the left hand side of Eq. (18) is of the same form of the right hand side of Eq. (13), and its right hand side is a function of known variables and can be readily calculated. So  $\varepsilon_a(\mathbf{q}, z')$ ,  $\varepsilon_b(\mathbf{q}, z')$  can then be solved in a similar way as in sec. (2A).

### 3. Simulation

For demonstration purposes, consider a semi-infinite turbid medium ( $z < 0$ ) with its surface at  $z = 0$  [Fig. (2)], whose absorption coefficient  $\mu_a = 0.0033\text{mm}^{-1}$  and reduced scattering coefficient  $\mu_s' = 1.0\text{mm}^{-1}$ .

Four absorbing objects A, B, C and D, each  $6.25\text{mm} \times 6.25\text{mm} \times 3\text{mm}$  and with absorption coefficient  $\mu_{a,\text{obj}} = 0.02\text{mm}^{-1}$  and reduced scattering coefficient equal to that of the background, are placed at depth 7.5mm, 7.5mm, 19.5mm and 19.5mm below the surface, and their  $xy$  coordinates are  $(-25, -18.75)\text{mm}$ ,  $(-12.5, -3.1)\text{mm}$ ,  $(9.4, 15.6)\text{mm}$  and  $(9.4, 6.25)\text{mm}$ , respectively. The medium is illuminated by an incident Gaussian pulse of a shape of  $\exp(-\rho^2/2\sigma^2)$  with  $\sigma = 50\text{mm}$  inside an

aperture of radius 50mm, propagating along negative  $z$ -axis at time  $t = 0$ .

These parameters are potentially applicable to optical mammography of the compressed-breast-toward-chest using backscattered photons. A series of measurements (total 15 snapshots from 300ps to 2400ps) of an area  $100\text{mm} \times 100\text{mm}$  on the surface plane  $z = 0$  are computed by using the direct calculation for the Gaussian pulse in  $\mathbf{r}$  space. The simulated data are used as input for inversion after adding a 1%, 5% or 10% Gaussian noise.

In the reconstruction part, the near-surface region of the turbid medium of depth up to 3 cm is sliced into  $N = 10$  layers, i.e.,  $\Delta z = 0.3\text{cm}$ , and objects A and B are then located on layer 3, C and D on layer 7. The detection plane of an area of  $10 \times 10\text{cm}^2$  is divided uniformly into a  $32 \times 32$  grid. Objects A, B, C and D all take  $2 \times 2$  elements by this grid. The results of reconstruction are shown below.

### A. Depth profile

The absorption depth profile, i.e. the total absorption perturbation per layer  $\int d^2\rho \delta\mu_a(\rho, z)$  vs depth  $z$  is shown in Fig. (3) with different noise levels for cases (a) 1% noise, (b) 5% noise and (c) 10% noise. In (a), there are one peak at depth  $z = 0.75\text{cm}$  (layer 3) where objects A and B are embedded, and another peak at  $z = 1.95\text{cm}$  (layer 7) where objects C and D are embedded. The width of the first peak at half height is 0.34cm, about the thickness of one layer (0.3cm), which means the depth of objects A and B is resolved very well. The second peak of objects C and D spans two and a half layers with its width of peak at half height 0.74cm, but its peak position is still correct.

When the level of noise increases, the peak values of both peaks decreases, and the half width increases. The effect on the second peak at  $z = 1.95\text{cm}$  is much more significant than that on the first one at  $z = 0.75\text{cm}$ .

## B. Layer reconstruction

The full 3D OPM is reconstructed. The reconstructed absorption coefficient of the layers at the two peak positions are shown in Fig (4), Fig. (5) and Fig. (6) for the three noise levels respectively. Fig. (4) shows objects A and B are clearly resolved as two objects centered at their original positions with negligible expansion; and objects C and D at depth  $z = 1.95\text{cm}$  are also detected at the correct central positions, but the resolved images are expanded on the  $xy$  plane. With the increase of noise level, the shape of objects A and B blurs from Figs. (4a) to (5a) and (6a), and the blur is even worse for objects C and D under the same condition (from Figs. (4b) to (5b) and (6b)).

The reconstructed absorption parameter for objects A and B is  $0.0071\text{mm}^{-1}$  at noise level 1%, about 36% of the original value  $0.02\text{mm}^{-1}$  of the absorptive inhomogeneity. In other words, the objects appears larger in space with a weakened absorption parameter. As the noise level increases, the effect is accentuated with a further reduction in the resolved absorption parameter.

## 4. Discussion

In the inversion part of the reconstruction, we have approximated the Gaussian wave by a simple plane wave. A refined solution could be obtained as discussed in sec. (2B). But it is not worth the effort, as our calculation shows the correction is less than 1% at layer 2.

The image reconstruction method provided is fast. The time it takes to perform an inversion in the above example (of  $32 \times 32 \times 10$  volume elements) is less than half a minute using a scripting language Python on one 180Mhz CPU of Origin 200 computer from Silicon Graphic Inc. This algorithm scales only linearly with the number of elements in the  $xy$  grid, so it can be used to handle larger data sets in real time with little difficulty.

This approach does not limit the number or the thickness of the inhomogeneities. It allows multiple inhomogeneities and one inhomogeneity may span several layers.

With little effort, a depth profile (the sum of the perturbation of optical parameter vs depth) of the inhomogeneities inside a highly scattering turbid medium can be obtained. This information may be very useful in some cases. When the inhomogeneity is found to exist only in one layer from the depth profile, the summation in Eq. (14) no longer exists. A direct inverse Fourier transform can thus be used to resolve the inhomogeneity when it is a sole absorptive or scattering perturbation.

### **Acknowledgment**

We thank Dr. W. Cai and Dr. S. Gayen for useful discussions and comments on this work. We also acknowledge DOE and USAMRMC for the support of this work.

## References

1. B. Chance and R. R. Alfano, eds., *Optical tomography, photon migration, and spectroscopy of tissue and model media: theory, human studies, and instrumentation*, Vol. 2389 of *Proc. SPIE* (1995).
2. R. R. Alfano, S. G. Demos, and S. K. Gayen, "Advances in optical imaging of biomedical media," *Ann. N. Y. Acad. Sci.* **820**, 248–271 (1997).
3. J. C. Hebden, S. R. Arridge, and D. T. Delpy, "Optical imaging in medicine: I. experimental techniques," *Phys. Med. Biol.* **42**, 825–840 (1997).
4. S. R. Arridge and J. C. Hebden, "Optical imaging in medicine: II. Modelling and reconstruction," *Phys. Med. Biol.* **42**, 841–853 (1997).
5. W. Cai, B. B. Das, F. Liu, M. Zavallos, M. Lax, and R. R. Alfano, "Time-resolved optical diffusion tomographic image reconstruction in highly scattering turbid media," *Proc. Natl. Acad. Sci. USA* **93**, 13561–13564 (1996).
6. X. D. Li, T. Durduran, and A. G. Yodh, "Diffraction tomography for biomedical imaging with diffuse-photon density waves," *Opt. Lett.* **22**, 573–575 (1997).
7. X. Cheng and D. A. Boas, "Diffuse optical reflection tomography with continuous-wave illumination," *Opt. Express* **4**, 118–123 (1998).
8. W. Cai, S. K. Gayen, M. Xu, M. Zavallos, M. Alrubaiee, M. Lax, and R. R. Alfano, "Optical tomographic image reconstruction from ultrafast time-sliced transmission measurements," *Appl. Opt.* **38**, 1–10 (1999).
9. T. Durduran, J. P. Culver, M. J. Holboke, X. D. Li, and L. Zubkov, "Algorithms for 3D localization and

imaging using near-field diffraction tomography with diffuse light," *Opt. Express* **4**, 247–262 (1999).

10. S. R. Arridge, "Photon-measurement density functions. Part I: Analytic forms," *Appl. Opt.* **34**, 7395–7409 (1995).
11. P. C. Hansen, "Analysis of discrete ill-posed problems by means of the L-curve," *SIAM Rev.* **34**, 561–580 (1992).

## List of Figures

1	A schematic diagram of inversion. . . . .	15
2	The geometry for time-resolved Fourier optical diffuse tomography using backscattered photons. The source is a picosecond (near) plane wave pulse, and a series of snapshots of a $10 \times 10\text{cm}^2$ area on the surface are computed as the input to image reconstruction. The absorptive objects A $(-2.5, -1.875, -0.75)\text{cm}$ , B $(-1.25, -0.31, -0.75)\text{cm}$ , C $(0.94, 1.56, -1.95)\text{cm}$ and D $(0.94, -0.625, -1.95)\text{cm}$ are used in the simulation. . .	16
3	The absorption depth profile for (a) with 1% noise, (b) 5% noise, and (c) 10% noise.	17
4	Layer reconstruction at a noise level of 1%: (a) resolved objects A (left) and B (right) at $z = 0.75\text{cm}$ (layer 3), and (b) resolved objects C (upper) and D (lower) at $z = 1.95\text{cm}$ (layer 7). The darkness of the pixel represents the resolved absorption coefficient in the unit of $\text{mm}^{-1}$ . . . . .	18
5	Layer reconstruction at a noise level of 5%: (a) resolved objects A (left) and B (right) at $z = 0.75\text{cm}$ (layer 3), and (b) resolved objects C (upper) and D (lower) at $z = 1.95\text{cm}$ (layer 7). The darkness of the pixel represents the resolved absorption coefficient in the unit of $\text{mm}^{-1}$ . . . . .	19
6	Layer reconstruction at a noise level of 10%: (a) resolved objects A (left) and B (right) at $z = 0.75\text{cm}$ (layer 3), and (b) resolved objects C (upper) and D (lower) at $z = 1.95\text{cm}$ (layer 7). The darkness of the pixel represents the resolved absorption coefficient in the unit of $\text{mm}^{-1}$ . . . . .	20

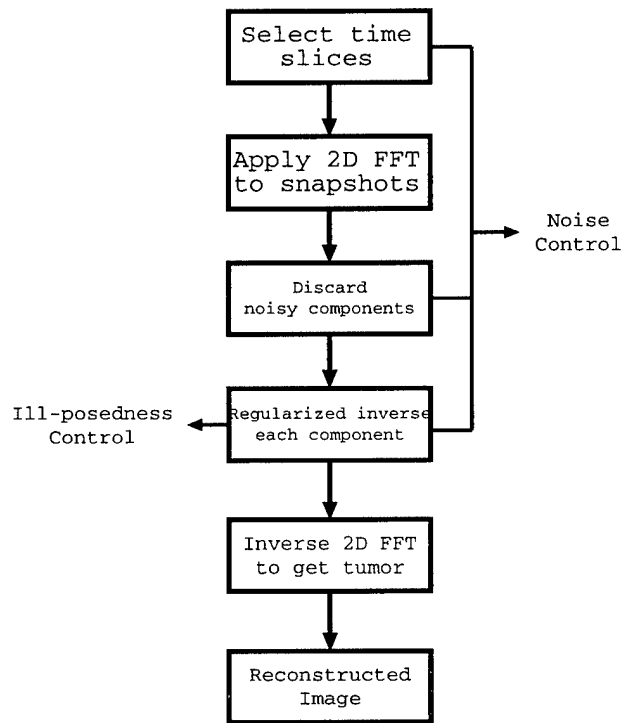


Fig. 1. M. Xu et. al.

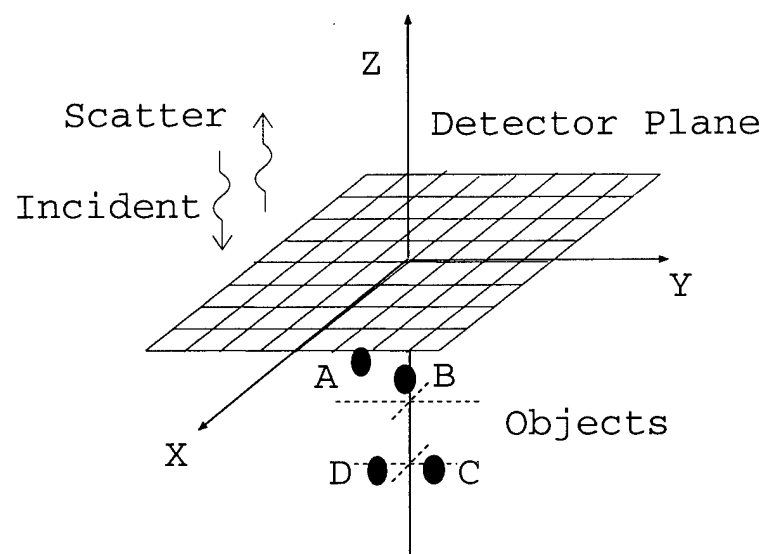
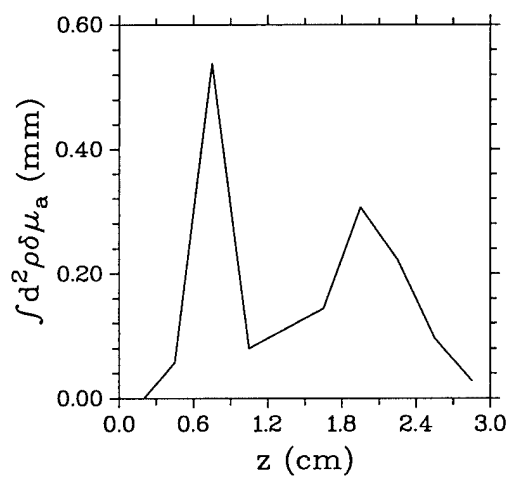
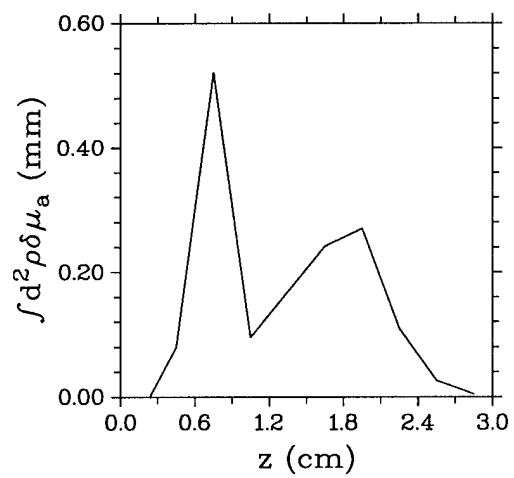


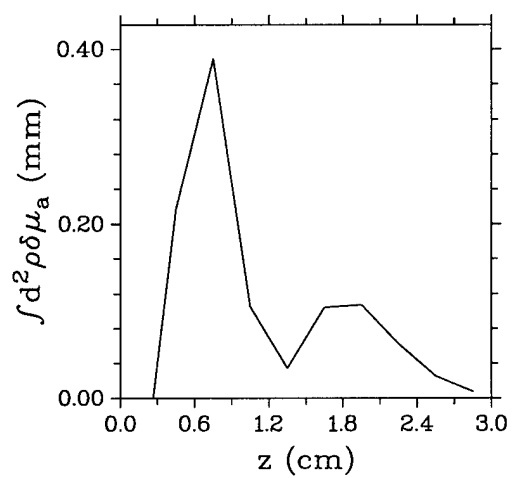
Fig. 2. M. Xu et. al.



(a)



(b)



(c)

Fig. 3. M. Xu et. al.

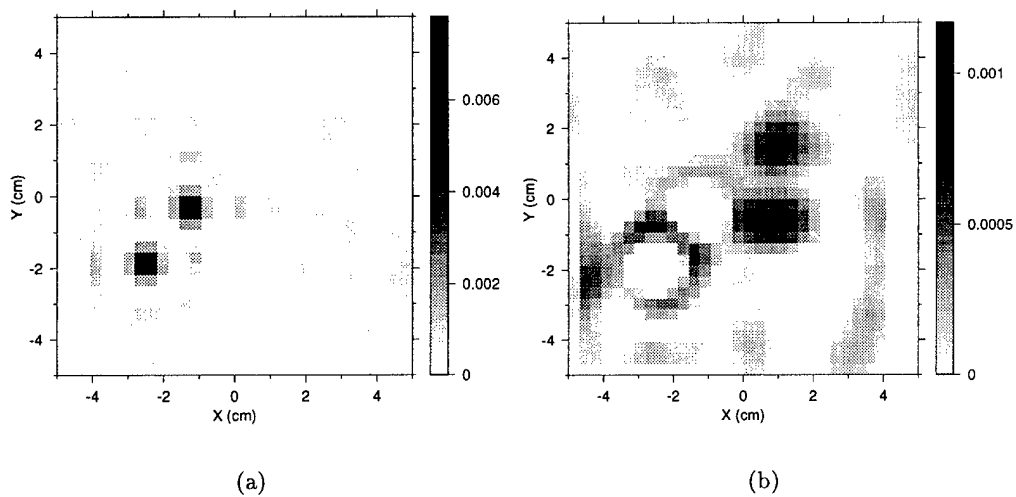


Fig. 4. M. Xu et. al.

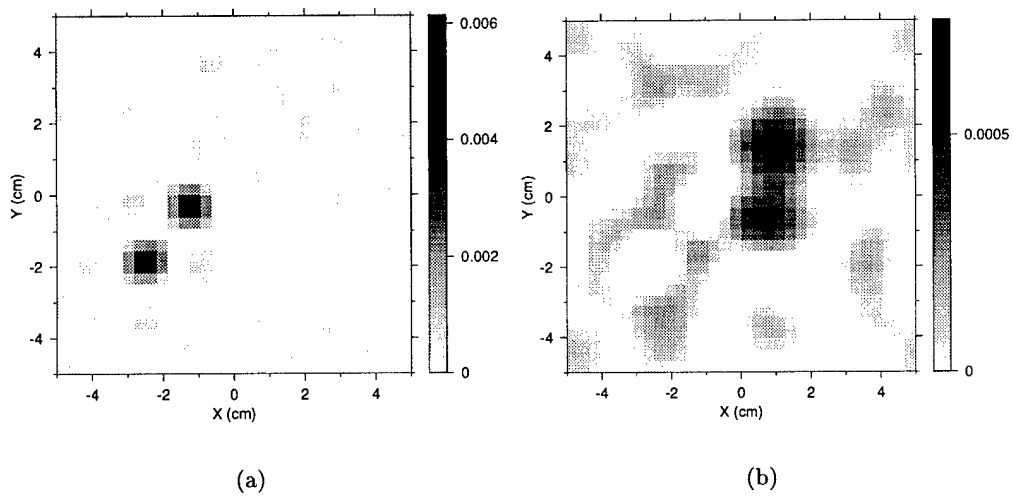


Fig. 5. M. Xu et. al.

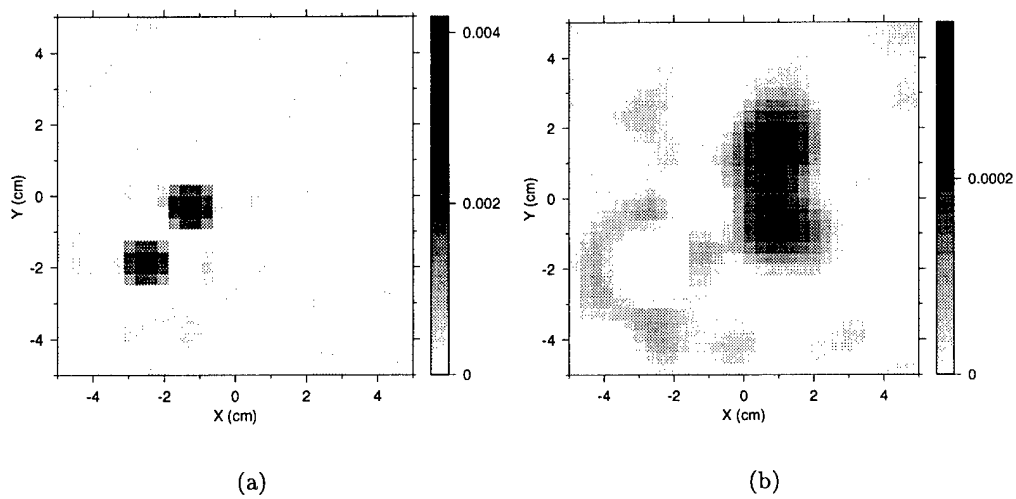


Fig. 6. M. Xu et. al.